

## Cosmological Implications of Galaxy Cluster Evolution

John C. Tsai

Canadian Institute for Theoretical Astrophysics  
 McLennan Labs, University of Toronto, 60 St. George St.  
 Toronto, Ontario, Canada, M5S 1A7  
 tsai@cita.utoronto.ca

David A. Buote<sup>1</sup>

Department of Physics and Center for Space Research 37-241  
 Massachusetts Institute of Technology  
 77 Massachusetts Avenue, Cambridge, MA 02139  
 dbuote@space.mit.edu

### ABSTRACT

We analyze with hydrodynamical simulations the evolution of galaxy clusters in a cosmological environment. Power ratios (Buote & Tsai 1995) are used to quantitatively relate cluster morphologies to their dynamical states. The simulated clusters follow the same “evolutionary track” obeyed by a sample of low-redshift ( $z < 0.2$ ) ROSAT PSPC clusters (Buote & Tsai 1996) indicating that the detailed evolution of individual simulated clusters is consistent with observed clusters. However, the distribution of simulated clusters (for  $\Omega = 1$  standard Cold Dark Matter) along the evolutionary track at the present epoch, which indicates a measure of the present balance of cluster formation and relaxation rates, suggests that there are too many simulated clusters with significant amounts of substructure to be consistent with the observations, thus favoring a lower value of  $\Omega$ . Perpendicular to the evolutionary track the distributions of observed and simulated clusters are consistent which may indicate a success of the cosmological model (e.g., power spectrum). Analysis of high-redshift simulated clusters suggests that the distribution of clusters both along and perpendicular to the evolutionary track is effectively constant from  $z \sim 0.6$  to the present but changes significantly for  $z > 0.6$ .

*Subject headings:* galaxies: clusters: general – galaxies: evolution – galaxies: structure – cosmology: theory

---

<sup>1</sup>Present Address: Institute of Astronomy, Madingly Road, Cambridge CB3 0HA, UK

## 1. Introduction

In a universe where structure formation occurs by hierarchical clustering, e.g. in the standard cold dark matter cosmogony (CDM), newly formed galaxy clusters should have complex morphologies with copious amounts of small-scale structure (i.e. “substructure”). If the cluster relaxation time is short ( $\lesssim$  Gyr), which is reasonable since the sound crossing and dynamical times are short, then the fraction of clusters which appear unrelaxed at a given epoch will reflect the cluster formation rate at that time. This rate likely depends upon the cosmological density parameter  $\Omega$  (e.g. Richstone, Loeb, & Turner 1992; Lacey & Cole 1993; Bartelmann, Ehlers, & Schneider 1993; but also see Kauffmann & White 1993; Nakamura, Hattori, & Mineshige 1995), thus the distribution of cluster morphologies provides a constraint on the density of the universe.

Alternatively, if structure formation proceeds by some other means, such as the fragmentation (top–down) picture of hot dark matter, cosmic strings, or textures, the morphology of clusters may also provide cosmological constraints. In the top–down scenario, for example, structures which are on the verge of fragmenting into smaller components should exhibit significant substructure. Hence the fraction of unrelaxed structures measures the “destruction” rate of these objects and this rate may relate to the underlying cosmology.

Implementing the above ideas requires a suitable measure of substructure which relates directly to the dynamical state of the cluster. The degree of virialization is well defined by the shape of the cluster potential: i.e. a spherically symmetric or moderately flattened potential implies a relaxed cluster whereas very distorted isopotential contours imply an unvirialized state (e.g., Buote & Tsai 1995 and Buote & Canizares 1996). The potential is characterized by a multipole expansion. The size of the lowest few terms of the expansion relative to the monopole term gives an indication of the distortions in the potential; very small scale structure represented by higher order terms in the expansion contributes negligibly to the overall cluster potential. Since three dimensional properties of individual clusters cannot be determined from observations, attention must be limited to the projected cluster potential and to its multipoles. The corresponding loss of information due to projection effects can only be recovered by considering a statistically large sample of clusters.

A measure of substructure based on expansions of the potential was introduced by Buote & Tsai (1995a; hereafter BTa). The two dimensional potential  $\Psi(R, \phi)$  due to material interior to projected radius  $R$  is expanded,

$$\Psi(R, \phi) = -2Ga_0 \ln\left(\frac{1}{R}\right) - 2G \sum_{m=1}^{\infty} \frac{1}{mR^m} (a_m \cos m\phi + b_m \sin m\phi), \quad (1)$$

where  $\phi$  is the azimuthal angle,  $G$  is the gravitational constant and,

$$a_m(R) = \int_{R' \leq R} \Sigma(\vec{x}') (R')^m \cos m\phi' d^2x', \quad (2)$$

$$b_m(R) = \int_{R' \leq R} \Sigma(\vec{x}') (R')^m \sin m\phi' d^2x'. \quad (3)$$

In the above,  $\Sigma$  is the projected mass density. The square of each term on the right hand side of eq. (1) integrated over the boundary of a circular aperture of radius  $R_{ap}$  is given by,

$$P_m = \frac{1}{2m^2 R_{ap}^{2m}} (a_m^2 + b_m^2) \quad (4)$$

for  $m > 0$  and

$$P_0 = [a_0 \ln(R_{ap})]^2 \quad (5)$$

for  $m = 0$ . The importance of the term of order  $m$  relative to the monopole term is given by the ratio  $P_m/P_0$  (dubbed a “power ratio”).

The above formalism implies that  $\Psi$  is specified by  $\Sigma(R, \phi)$ , which can be determined in principle from weak lensing measurements (e.g., Kaiser & Squires 1993). However,  $\Sigma(R, \phi)$  is only available for  $\sim 5 - 10$  clusters and is given over relatively small regions of the cluster ( $\sim 0.4h_{50}^{-1}$  Mpc; Squires et al. 1995 and references therein). A more readily available tracer of the distribution of matter must instead be used for statistical analysis. A possibility is the projected density of galaxies in the cluster. Although previously used to study cluster structure (e.g., Geller & Beers 1982; Dressler & Shectman 1988; West & Bothun 1990), the method is fundamentally limited by the finite number of galaxies ( $N \sim 1000$ ) in each cluster. Alternatively, the X-ray surface brightness profile  $\Sigma_x$  traces the projected X-ray emission measure. For instruments such as the ROSAT Position Sensitive Proportional Counter (PSPC; Pfeffermann 1987), this translates into the projected square of the gas density  $\rho^2$  since the emissivity in the specified observing band for clusters is nearly constant. Replacing  $\Sigma(R, \phi)$  with  $\Sigma_x$  in eqs. (2) and (3) implies that the expansion in eq. (1) will not give precisely the potential  $\Psi$ , but some related quantity which would still specify the dynamical state of the cluster provided the X-ray emission qualitatively traces the mass distribution (BTa and see below for explicit tests of this relation). The abundance of high quality X-ray imaging data over large regions of observed clusters, especially from ROSAT, currently makes  $\Sigma_x$  the most attractive tracer of cluster mass.

Buote & Tsai (1996; hereafter BTb) computed power ratios for a sample of 59 clusters observed by the ROSAT PSPC. The primary purpose of this study was to construct a large data set suitable for statistical studies of cosmology. However, the data also exhibited several interesting properties and correlations which may have significant implications for cluster evolution. The expansion coefficients  $a_m$  and  $b_m$  were computed on fixed apertures of  $R_{ap} = 0.5, 1.0, \text{ and } 1.5$  Mpc (we assume  $H_0 = 80 \text{ km s}^{-1} \text{ Mpc}^{-1}$  for the remainder of this paper) with the center of the aperture defined by, (i) the centroid of the image (where  $P_1 = 0$ ), and (ii) the emission peak. These latter power ratios are denoted  $P_m^{(pk)}$  to distinguish them from those of case (i). We compute the power ratios in fixed apertures to enable consistent comparison of structures of the given scale. This procedure is a key aspect of the power ratios: the scale of substructures being probed is set by the aperture size so that different information is generally provided by power ratios computed in apertures of different sizes (BTa).

The set of ratios  $P_m/P_0$  (with 1 Mpc apertures defined about the centroid) for  $m = 2, 3$ , and 4 define the axes of a three dimensional space in which each cluster occupies a unique position (we actually use  $\log(P_m/P_0)$  for the axes). Those clusters with significant non-axisymmetric structure will generally have larger values of  $P_m/P_0$  so will occupy the region far removed from the origin of the coordinate system. Conversely, relaxed clusters will congregate around the origin. BTb found that observed clusters of varying morphologies occupied only a restricted region in the space defined by the power ratios, lying basically in a thick straight filament extending outwards from the origin. The projection of this filament onto the three coordinate planes implies significant correlations among the three power ratios. In particular, the correlation between  $P_2/P_0$  and  $P_4/P_0$  is rather strong and admits a physical interpretation. Recently formed clusters arrive on the correlation line with large values for the power ratios. As structure is erased by relaxation, the cluster moves down the correlation line towards the origin, finally coming to rest near the origin as a virialized cluster. Of course, clusters can also move upward toward large power ratios if, for example, the cluster accretes or merges with a companion previously outside the aperture being considered. The correlation line (or indeed the thick filament in the three dimensional space) is interpreted as the “evolutionary track” followed by clusters as they relax and age. The position along this track specifies a measure of the dynamical state of the cluster and the distribution of clusters along the track provides a measure of the balance of the formation and relaxation rates for the clusters (see §3.2.). This distribution should be sensitive to  $\Omega$  (see above).

In this paper, we use N-body/Hydrodynamical simulations of cluster formation in the  $\Omega = 1$  CDM cosmogony (Navarro, Frenk, & White 1995; hereafter NFW) to (i) understand the correlations of the observed power ratios and test the evolutionary track interpretation of the correlation line, (ii) determine if clusters formed in an  $\Omega = 1$  CDM cosmogony are similar in structure to real clusters, (iii) to assess the cosmological implications of the observed distribution of power ratios, and (iv) to study the the evolution of power ratios with redshift in an  $\Omega = 1$  CDM cosmogony. The cosmological consequences of substructure have been previously considered by several groups (e.g., Evrard et al. 1993, Mohr et al. 1995; Jing et al. 1995) using a different set of statistics from the power ratios (e.g., centroid shifts, axial ratios, orientation angles, and radial falloff). While Mohr et al. indicate that the  $\Omega = 1$  CDM model is preferred over low  $\Omega$  models, Jing et al. reach the different conclusion that an  $\Omega = 0.3$ , flat model appears to work equally well as the  $\Omega = 1$  case. Although similar statistics are used, the reasons for the discrepancy are not clear. Some differences are that the apertures over which the statistics are computed are not treated the same way and Jing et al. use a hydrostatic model for putting gas into purely dissipationless simulations, whereas Mohr et al. use gas-dynamical simulations. Clearly, an independent set of statistics should be applied to the problem to check previous results. This is also important, however, because the previously used statistics are not clearly related to the dynamical state of the cluster (see BTa), although they do represent a means of quantitatively classifying the structures present. For example, it is not obvious that centroid shifts and axial ratios admit an interpretation in terms of the evolutionary track discussed above. The X-ray data used (*Einstein* IPC images) also have inferior spatial resolution and signal-to-noise ratios to the

ROSAT data considered in BTb.

In §2., we briefly discuss the simulations and our method of analysis. The results for an aperture of 1 Mpc are presented in §3.. The power ratios computed on the dark matter distribution are compared with those for the gas in §4.. A discussion and conclusions are given in §5.

## 2. Method

The simulations are a combined N–body/SPH calculation of 6 clusters with velocity dispersions spanning the typically observed range,  $v \sim 400 - 1300 \text{ km s}^{-1}$ . The initial conditions for the cluster simulation were selected from a large N–body simulation without bias regarding the morphology of the cluster at the present time (specified by  $\sigma_8 = 0.63$ ). The baryonic fraction is assumed to be  $\Omega_b = 0.1$ . Cooling is not included in the simulations so structures in the densest regions (cluster cores) are not well modeled. This is, however, not a problem since we never consider scales much smaller than  $r \sim 100 \text{ kpc}$  which is in any event roughly the gravitational softening length of the simulations. See NFW for a detailed description of the simulations.

We simulate observations of each cluster along three orthogonal axes with random orientation. The X–ray surface brightness is computed,

$$\Sigma_x(R, \phi) = \int_{-\infty}^{\infty} \Lambda_x [T(R, \phi, z)] \rho^2 dz, \quad (6)$$

where  $\rho$  is the gas density,  $R$  and  $\phi$  specify the location in the observed plane, and  $z$  is along the line of sight. The quantity  $\Lambda_x$  is the cluster emissivity convolved with the spectral response of the PSPC. Although the atomic X–ray emissivity of the gas generally varies with gas temperature, the PSPC convolved emissivity is constant to a very good approximation for the clusters considered here (most cluster gas is hotter than  $\sim 1 \text{ keV}$  where the PSPC is most sensitive; see NRA 91-OSSA-3, Appendix F, ROSAT mission description). We take  $\Lambda_x$  to be strictly constant, and since we consider exclusively ratios of  $P_m$ , the exact numerical value of  $\Lambda_x$  is immaterial. Reasonable amounts of Poisson noise and undetected point sources have no effect on the computed  $P_m$  (see BTa) so are not included in constructing the synthetic observations.

The power ratios are computed from  $\Sigma_x$  for each of the projections and for a variety of redshifts  $z$  in an aperture of radius 1.0 Mpc in order to test the “evolutionary track” idea. Although we also compute the power ratios for an aperture size of 0.5 Mpc, these results are in every way qualitatively similar to those with the larger aperture so are not presented in this paper. Furthermore, there are too few observed clusters with well determined  $P_m/P_0$  for an aperture size of 1.5 Mpc to be considered. We note that other choices for  $R_{ap}$  are possible: for example, the virial radius as fixed by the temperature of the X–ray emitting gas. As noted in BTa, however, there are significant difficulties with this latter approach. Uncertainties in the

temperature imply large uncertainties in the determined virial radius. This potentially masks the information contained in the distributions of power ratios. Secondly, typical virial radii are large enough that in many cases there is insufficient available data to accurately compute the power ratios. We therefore restrict  $R_{ap}$  to fixed metric distances.

### 3. Results for a 1 Mpc Aperture

#### 3.1. Cluster Evolution and the Evolutionary Track

In this section we describe the morphological evolution of the NFW clusters to examine how the dynamical states of the clusters are indicated in terms of the power ratios, and to test the “evolutionary track” interpretation of BTb. The evolution of the largest simulated cluster (cluster CL1 in the notation of NFW) is shown in Figures 1, 2, and 3. The SPH gas particles are plotted as viewed along the three orthogonal directions  $x$ ,  $y$ , and  $z$ . The evolution of the cluster is typical for bottom–up structure formation scenarios. At early times, the cluster is a loose aggregate of small clumps which are growing constantly by accreting surrounding gas (and dark matter). At  $z = 0.49$  two of the clumps merge followed by the final merger event somewhere between  $z = 0.49$  and  $z = 0.35$ . The subsequent evolution of the cluster is simply that of a single clump achieving hydrostatic equilibrium while incrementally growing by the slow accretion of adjacent material. We only show this cluster in detail since the evolution and growth of the other clusters proceeds basically in the same manner as described above, although the morphology at  $z = 0$  is generally very different from that of CL1 (see NFW).

Some of the power ratios computed for this cluster for an aperture size of  $R_{ap} = 1$  Mpc are shown in Figures 4 and 5. The heavy solid lines indicate the limited region of  $P_m$  space occupied by observed clusters (hence the observed correlation among the  $P_m$ ). These are simply made by joining the ends of several of the error bars from Figure 4 of BTb; it is only meant to give a rough idea of the observed values of  $P_m$ . We consider each projection in turn to understand variations in the  $P_m$  due to both cluster evolution and differing viewing directions.

##### 3.1.1. Power Ratios for Three Different Projections

At the earliest redshift  $z = 1.4$ , the cluster viewed along the  $x$  axis has widely separated clumps. We define clumps as belonging to the same cluster if they satisfy the following condition. The surface brightness profile  $\Sigma_x$  of each clump is circularly averaged about the local peak of  $\Sigma_x$  to yield a radial profile. If any point on the annulus which has  $\Sigma_x$  equal to 1% of the peak value

is within 1 Mpc of the emission peak of another clump, then those two clumps are considered part of the same cluster. For two given clumps, if the previous condition is valid for annuli of either clump, they are considered part of the same cluster. Although more arbitrary than some dynamically motivated condition, this definition allows a consistent comparison of theory to observations provided the latter are subject to the same criteria. This definition also does not require perhaps dubious dynamical modeling of the cluster.

The 3 major clumps at  $z = 1.4$  are considered separate clusters by the above definition, although after subsequent mergers the distinction disappears. The power ratios shown in the figures are computed for the central clump. The morphology is “boxy” or elongated along the four filaments extending from the clump and there is considerable small scale structure compared to the overall ellipticity of the clump. This is reasonable considering the clump recently formed out of diffuse matter and is not yet virialized. Corresponding to these properties, the values of  $P_4/P_0$  and  $P_3/P_0$  are above average for the amount of  $P_2/P_0$  present and the clump sits at the upper boundary of the region occupied by observed clusters. Although the  $P_2/P_0$  value is reminiscent of a cluster like A545 (see BTb) which is highly elongated, there is considerably more higher order structure than in A545. By the next redshift  $z = 0.95$ , the central clump has relaxed and the higher order non-axisymmetric structures are erased. All the ratios decrease and the cluster moves into the region of  $P_m$  space occupied by virialized, regular clusters such as A2029. At  $z = 0.68$ , the three clumps are still considered separate, however, because they have moved closer together the structures linking the clumps move into the aperture and contribute to an increase in the power ratios.

Shortly after  $z = 0.68$ , one of the other clumps moves into the aperture of the central clump and the two gradually merge. The next redshift considered ( $z \sim 0.49$ ) shows the final stages of this merger. The cluster morphology implies a large quadrupole moment  $P_2/P_0$ , but not a large value of  $P_3/P_0$ . The latter result occurs because the two clumps in the merger are nearly equal-sized so there is little structure that is symmetric with respect to rotations of angle  $2\pi/3$  about the origin –  $P_3/P_0 = 0$  for bimodals with exactly equal-sized clumps (BTa). Note that the evolution of the power ratios in time does not necessarily follow the dashed lines in Figures 4 and 5; these lines simply emphasize the sequence of circles which capture the cluster structure at a fixed set of redshifts. For example, the entire merger sequence has been missed because of the discretely spaced coverage of redshifts. In actuality, the power ratios must become very large and move to the upper right of the power ratio plots when the merging cluster is a bimodal with widely separated clumps. As the clumps coalesce, the power ratios move back down towards the lower left. The motion of the cluster in power ratio space is thus more complex than indicated simply by the dotted lines, although we know that the merger time is short because the merger happens between two closely spaced redshifts. The above merging sequence will be clearly seen below for the  $z$  projection.

The merger with the last subclump has occurred by  $z = 0.35$ . Although the cluster shows remaining morphological signs of the event, it has already relaxed appreciably as is indicated by

the smaller power ratios. At  $z = 0.23$  the power ratios grow again because of the accretion of small surrounding lumps, for example, the gas in the upper left corner in panel (e) of Figure 1. The remaining relaxation and continued slow accretion of surrounding material until  $z = 0$  causes the power ratios to change somewhat but they remain in the region occupied by relaxed clusters.

The same considerations can be applied to the other projections. Several forming clumps are again seen at the earliest redshift when the cluster is viewed down the  $y$  projection. The clumps are separate according to our criterion (see above) so for now we plot power ratios of the central clump. This clump is unvirialized as it exhibits substantial small-scale structure. Correspondingly, the values of the higher order power ratios are large in proportion to the value of  $P_2/P_0$  and the clump sits above the upper boundary of the region occupied by observed clusters in Figures 4 and 5. The clump quickly relaxes so that by redshift  $z = 0.95$  the power ratios correspond to that of a regular cluster. By the next redshift, the upper clump has moved sufficiently within the aperture of the central clump so that the power ratios become large and the cluster moves to the upper right in the  $P_m/P_0$  plots. The “cluster” now consists of both the central clump and the upper clump which were initially considered distinct. This contrasts with cluster properties when viewed down the  $x$  axis. In that case, the clumps were still sufficiently far apart to be considered separate clusters hence the power ratios were computed for only the central clump.

The relaxation and merger of the bimodal cluster at  $z = 0.68$  has occurred by the subsequent redshift. From the  $x$  projection, we know that although the merger is almost complete, two subclumps are clearly visible (panel [f] of Figure 1). However, the two lumps are along the line of sight when viewed in the  $y$  direction, hence the power ratios are smaller than in the  $x$  projection. The merger with the remaining secondary lump is complete by  $z = 0.35$  so this final merging sequence is not captured in the plots of  $P_m/P_0$ . Furthermore, the cluster at  $z = 0.23$  appears more relaxed in the  $y$  direction than in the  $x$  direction so it has correspondingly smaller power ratios. The evolution from this time to  $z = 0$  is again the virialization of the final cluster.

At the earliest redshift in the  $z$  projection, the topmost and central clumps are sufficiently close to be considered a single cluster on which we focus attention. This is a bimodal cluster with widely separated components of approximately equal size. The evolution to  $z = 0.49$  is simply the relaxation of this bimodal cluster as the two clumps draw closer together and merge. At  $z = 0.49$ , the last clump also falls into the aperture and the cluster again becomes a bimodal but with a smaller secondary clump. The cluster evolves in  $P_m/P_0$  space by sliding down the correlation line in either the  $P_4/P_0 - P_2/P_0$  plane or the  $P_3/P_0 - P_2/P_0$  plane, confirming the interpretation of an “evolutionary track” followed by clusters. After this time, the simulated cluster remains in the region occupied by single-component clusters as continues to evolve quasi-statically.

### 3.1.2. Physical Interpretation of the Power Ratios



We interpret physically the above detailed descriptions of cluster evolution in the CDM cosmogony as quantified by the power ratios. Unrelaxed single component clusters, such as the simulated cluster at  $z \sim 1.4$ , have significant amounts of smaller scale structure, which manifests itself as large values of the higher order power ratios  $P_4/P_0$  and  $P_3/P_0$  relative to  $P_2/P_0$ . These clusters appear in the power ratio plots in the upper region or above the area occupied by most observed clusters. As they virialize, they drop down to the region occupied by relaxed clusters at the lower left hand corner of the  $P_m/P_0$  plots. If the clump merges with another relatively massive clump, the cluster then moves to the upper right part of the  $P_m/P_0$  plots regardless of the individual states of relaxation of the clumps. As the clumps merge, the cluster slides down the correlation line (which has a finite thickness; more about this below) towards the lower left where the power ratios are small. Multiple mergers during the lifetime of a cluster are certainly possible and likely in the CDM cosmogony. Thus the clusters can move up and down the correlation line many times in the course of their lives. These properties allow us to assess the evolutionary state (in projection) of any given cluster based on its location in power ratio space. For example, unrelaxed single clusters invariably appear in the upper part of the correlation line. Examples of this may include A665 and Cygnus-A (see BTb).

The evolution of any individual cluster can appear differently depending on viewing direction. Clumps that are truly widely separated ( $r_{sep} \gtrsim 3$  Mpc) may either appear separated enough to be considered two distinct clusters, or appear closely associated and taken to be a single cluster. Similarly, the merger rate for a given cluster can significantly differ if in one projection the secondary clump is outside the aperture whereas in another it is within the aperture. Thus, in any comparison of simulations to observations a statistically large number of clusters must be averaged over to obviate projection effects. In any case, it is important to select clusters from observations and simulations in a consistent fashion to ensure that each sample is similarly affected by projection effects.

The interpretation of the correlation line in power-ratio space as an evolutionary track, however, applies regardless of the orientation of the cluster. It is simply a quantitative representation of the evolution of the cluster when viewed in the given direction. (Note that projection effectively smoothes the intrinsic three-dimensional mass distribution of a cluster, hence the power ratios in a given projection provide a lower limit to the true dynamical state. A cluster is no more virialized than indicated by its power ratios.) We stress that one of the great assets of the power ratios is the ability to consistently compare the structures and evolutionary states of clusters of very different sizes. For example, the clumps appearing at  $z = 1.4$  in the simulation are much less massive than are the final clusters, however, the power ratios allow for a consistent relative comparison of the two clusters because the overall surface brightness does not enter into the ratios  $P_m/P_0$ .

An intuitive understanding of the evolutionary track may be obtained by considering simple analytic models for galaxy clusters. Figure 6 shows the  $P_4/P_0$ – $P_2/P_0$  plane along with the region occupied by observed clusters. We plot the power ratios of single component  $\beta$  models (e.g.,

Cavaliere & Fusco-Femiano 1976),

$$\Sigma_x(R) \propto \left[ 1 + \left( \frac{R}{a_{core}} \right)^2 \right]^{-3\beta+1/2}, \quad (7)$$

where in order to incorporate models with constant ellipticity  $\epsilon_x$  we take  $R^2 = x^2 + y^2/q^2$  assuming  $q$  is a constant axis ratio. We expect that an ellipsoidal distribution with high ellipticity will relax to a more spherically symmetric distribution (assuming rotation and anisotropic pressure are dynamically unimportant for the gas). Assuming standard values of  $\beta = 0.75$  and  $a_{core} = 0.3$  Mpc (e.g., Jones & Forman 1984), we plot the power ratios assuming  $\epsilon_x = 0.6, 0.3, 0.2$ , and  $0.1$ . Higher ellipticities correspond to larger power ratios. The expected evolutionary behavior of a simple model translates into a path in power ratio space very similar to the true evolutionary track for clusters with a slope that is slightly steeper than the track followed by the detailed simulations.

To understand this behavior we consider single-component  $\beta$  models with  $\beta = 0.75$  but  $a_{core} = 0.1$  Mpc. These are indicated by the filled circles in Figure 6. Again, the evolution from large to small ellipticities translates into decreasing power ratios along a line that is steeper than the evolutionary track. The line followed by the model clusters, however, is displaced relative to larger core radius case. A bimodal cluster model composed of two spherical  $\beta$  model components each with  $\beta = 0.75$  and  $a_{core} = 0.3$  Mpc separated by distance  $r_{sep}$  evolves along a similar track as  $r_{sep}$  decreases (the open stars of Figure 6). Although each of the preceding models exhibits the correct qualitative behavior, the detailed slopes are incorrect. An explanation for this is that clusters likely will not simply become rounder, in the case of a single component cluster, or have unchanging clumps approaching each other in the case of a bimodal cluster. Up to a point, general relaxation tends to concentrate mass distributions as well so that the parameters describing the mass distributions are likely to evolve also. As an illustration, consider the path followed in power ratio space if a single  $\beta$  model cluster with  $\beta = 0.75$ ,  $a_{core} = 0.3$  Mpc,  $\epsilon_x = 0.6$  evolves to a cluster with smaller  $\epsilon_x = 0.3$ , but also smaller  $a_{core} = 0.1$  Mpc. This is given by joining the topmost open circle with the topmost filled circle of Figure 6. The slope is a better match to that of the evolutionary track suggesting that indeed cluster evolution is accompanied by specific changes in cluster parameters, such as the core radius and the ellipticity. This issue is considered in more detail in §3.4.

### 3.2. Statistical Comparisons at Low Redshift ( $z < 0.1$ )

The distribution of clusters along the evolutionary track is determined by the balance between the cluster relaxation and formation rates, and hence isolates the information which likely specifies  $\Omega$ . In keeping with our phenomenological approach (see BTb), we make the following intuitive definitions of these rates guided in part by results from the preceding section. We consider the

“relaxation rate” to be defined as the hypothetical rate at which clusters would move down the evolutionary track in isolation; i.e. when undisturbed by mass accreting from outside the specified aperture. The “formation rate” consists of two components, a “birth rate” and “merger rate”. The birth rate is the rate at which clusters first appear on the upper parts of the track immediately after forming out of the background matter. In contrast, the “merger rate” is the rate at which a mature cluster jumps from a lower position to a higher position on the track due to the accretion of mass from outside the specified aperture. If these rates as described in terms of movement along the evolutionary track are in fact physically similar to typical theoretical constructions (e.g., Richstone et al. 1992; Lacey & Cole 1993; Bartelmann, Ehlers, & Schneider 1993; Kauffmann & White 1993; Nakamura, Hattori, & Mineshige 1995), then this would suggest that to probe  $\Omega$  effectively we should consider the location of clusters in power-ratio space relative to a set of rotated coordinates where one axis lies along the correlation line.

In order to make use of all the information provided by the power ratios, it is also important to consider the distribution along an axis perpendicular to the evolutionary track. In essence, for a given point on the evolutionary track a cluster lying perpendicularly to the left of the track possesses a larger amount of smaller scale structures (i.e. excess  $P_3/P_0$  or  $P_4/P_0$ ) but a less pronounced aggregate, larger scale structure (i.e. less  $P_2/P_0$ ); the opposite is true for clusters lying perpendicularly to the right of the track. Hence, the distribution of clusters perpendicular to the evolutionary track is probably not intimately related to the rates of relaxation and formation described above and is thus unlikely to be strongly dependent on  $\Omega$ . However, the perpendicular distribution may provide different, yet potentially equally interesting, constraints on the structure of clusters. For example, the perpendicular distribution would seem to be related to the shape of the power spectrum of initial fluctuations on cluster scales (if that information is preserved during cluster evolution), or to the manner of cluster relaxation (such as by gravitational/pressure forces). Whether such effects are indeed important will require further study (see Buote & Xu 1996). Finally, the slope and intercept of the correlation line itself may be related either to the specifics of cluster evolution or to the cosmological model.

Figure 6 shows the “best measured” clusters from the ROSAT sample of BTb (error bars are excluded to avoid clutter). These clusters are defined to have error bars that span less than a decade except for those with  $P_4/P_0$  or  $P_2/P_0$  values  $\leq 0.25 \times 10^{-7}$ . This gives a sample of 31 clusters. The light solid line shows the best fit line to these data and is given by  $\log(P_4/P_0) = a + b \log(P_2/P_0)$  with  $a = -0.86 \pm 0.4$  and  $b = 1.188 \pm 0.077$  where standard errors are indicated. This best-fit line is adopted for the evolutionary track. (Note that the parameters of this best-fit correlation line and those that follow are changed negligibly when instead all clusters corresponding to the augmented Edge et al. 1990 sample are used in the fits – Buote & Xu 1996.)

We transform the coordinates from the power ratios ( $P_2/P_0, P_4/P_0$ ) (specifically, the log of the power ratios) to a system  $(x_p, y_p)$  oriented such that the  $x_p$  axis coincides with the best-fit line above and the  $y_p$  axis is perpendicular to  $x_p$ . The origin of the new coordinates is set to  $\log(P_2/P_0) = -8.0$  and  $\log(P_4/P_0) = -10.37$ . Figure 7 shows the distribution of clusters when

referred to the new coordinate system where  $x_p$  and  $y_p$  are both measured in log units. The distributions for two sets of data samples are shown. Out of a total of 59 clusters considered, 44 had power ratios that could be determined for a 1 Mpc aperture (see BTb). This sample is shown by the heavy solid histogram. The distribution of the “best observed” 31 of these clusters is given by the light solid histogram and that of the simulated clusters by the dashed histogram.

We construct the simulated cluster sample by combining the power ratios of the three projections (see §2.) of each of the simulated clusters for the two lowest redshifts considered,  $z = 0$  and 0.07, which correspond approximately to those of the observed cluster sample. This assumes that each projection of a given cluster represents an independent observation for the purposes of statistical analysis, i.e., each simulated cluster represents the “average” cluster of that size and the process of observing is simply viewing that cluster from random angles. This is standard practice in those cases where small numbers of simulated clusters are available (e.g., Evrard et al. 1993, Mohr et al. 1995). We further assume that a given cluster can be considered independent at two different (but close) times in its evolution. Although each simulated cluster originates from a single fluctuation in the initial matter distribution, every cluster passes through a similar series of morphological stages during its evolution (based on the simulations). Hence the observation of a number of clusters of the same mass is equivalent to observing one cluster but picking it out at several different stages in its evolution. Although there are still really six independently simulated clusters, provided the forgoing assumptions are not grossly inaccurate, the augmented sample of simulated clusters will allow for interesting quantitative comparison with the sample of ROSAT clusters. In any case, the conclusions drawn below do not change if only one specific redshift is considered.

In constructing the sample of simulated clusters, equal weight is assigned to each cluster. Ideally, we must ensure that the contents of the model sample agree with constraints from the luminosity function and the limiting flux of the ROSAT sample we use for comparison. We find, however, that in a flux-limited sample corresponding to the ROSAT data and the observed luminosity function of ROSAT clusters (e.g., Briel & Henry 1993) the abundances of clusters with masses represented by the simulated clusters will indeed be uniform. Hence the assignment of equal weights to each of the clusters does indeed give a distribution of clusters (in mass) that approximately replicates the observed distribution.

The distributions for the data and for the simulations in the  $x_p$  direction are inconsistent. The simulated clusters are distributed more uniformly over the evolutionary track than the ROSAT sample and exhibit an excess of large  $x_p$  clusters; i.e. the simulated clusters have more substructure on the indicated scale ( $\sim 1$  Mpc) than is found in the data. As a quantitative measure of this disagreement, a Kolmogorov-Smirnov (KS) test applied to the observed and simulated samples (again with the simulated sample constructed as described above) gives a probability of  $P(\text{KS})=4.4\%$  that the two samples arise from the same distribution.

This result appears similar to the result of one of the statistics used by Mohr et al. (1995)

who found that their measures of axial ratios were more broadly distributed for a sample of Einstein IPC clusters than for the  $\Omega = 1$  simulations. However, interpretation of the Mohr et al. result is unclear because the same cluster scales are not consistently compared – see BTa §6. for a discussion. (The other statistics used by Mohr et al. (1995), the centroid-shift and radial fall-off, were found to be essentially *consistent* for the  $\Omega = 1$  simulated clusters and IPC X-ray clusters.)

Assessing the sensitivity of this result to the incompleteness of the simulated cluster sample cannot be definitely answered with present simulations. However, a study in progress with purely dissipationless simulations shows that qualitatively the above conclusions are still obtained when a statistically large and independent sample of clusters is used (Buote & Xu 1996). Here, we consider the sensitivity of this conclusion to incompleteness in the data sample. The observed clusters comprise a sample which is  $\sim 50\% - 60\%$  complete for the brightest 35 clusters (BTb). Clusters with fluxes above the limiting value were missed for various reasons including instrument mispointings, images that were too large to fit inside the PSPC ribs (see BTb), and because they simply were not observed with the PSPC. Since clusters were not excluded for reasons related to their morphology, the missing clusters should have a distribution of power ratios similar to the observed sample. This expectation is supported by available information on the missing clusters. For example, the 1 Mpc aperture for some of the clusters in the data sample did not fit within the inner ring of the PSPC. In many cases, however, a significant fraction of the 1 Mpc aperture ( $\gtrsim 0.75$  Mpc) did fit within the ring which allows us to approximate the 1 Mpc value. Also, a qualitative assessment of the cluster structure is possible by visual examination of the emission in the 1 Mpc aperture lying outside the inner ring (BTb). Some of the clusters not observed by the PSPC were observed by the *Einstein* Imaging Proportional Counter (IPC) from which the cluster morphology can also be examined. Using both power ratios in apertures of radii  $0.75 \lesssim R_{ap} < 0.9$  Mpc and/or visual examination of available data for the missing clusters we find that not only is the distribution of power ratios similar to that shown in Figure 7, but that only  $\sim 2$  out of  $\sim 40$  clusters have power ratios in the region  $x_p \gtrsim 4.5$  where the disparity with simulated clusters is most severe.

A further demonstration of the stability of the distribution of observed clusters is provided by the sample of “best measured clusters.” These were not selected on the basis of their morphology but only on the size of the random errors associated with the observation. The distribution of these clusters should be similar to that of the larger sample, which is demonstrated by Figure 7. Similarly, if we consider only the  $\sim 35$  brightest clusters which comprises a sample that is  $\sim 50\% - 60\%$  complete (see BTb) then we obtain qualitatively similar distributions. Again as a simple measure of this similarity, we get  $P(\text{KS})=3\%$  in the  $x_p$  direction, consistent with the results for the whole sample.

The distributions in the  $y_p$  direction are consistent as indicated by the large probability  $P(\text{KS})=32\%$ ; again, this result holds for subsets of the data sample where, e.g., the  $\sim 35$  brightest clusters give  $P(\text{KS})=55\%$ . Intuitively this result implies that for a particular dynamical age (i.e. at a particular position along the evolutionary track) simulated clusters in the  $\Omega = 1$  simulation

tend to “look” like real clusters. This correspondence may represent a success of the cosmological model (see above and §5.).

The  $P_3/P_0 - P_2/P_0$  plane can be examined in the same way as above. We fitted a straight line to the evolutionary track given by the “best measured” clusters of Figure 5 resulting in  $\log(P_3/P_0) = a + b \log(P_2/P_0)$  where  $a = -1.81 \pm 0.58$  and  $b = 0.991 \pm 0.11$  with standard errors. As before, define the  $x_p$  and  $y_p$  axes to lie along and perpendicular to the best-fit line, respectively, and set the origin of the new coordinate system at  $\log(P_2/P_0) = -8.0$  and  $\log(P_3/P_0) = -9.07$ . The distribution of clusters relative to  $(x_p, y_p)$  are shown in Figure 8 where the coordinates are measured in log units.

The results in this case are consistent with those from the  $P_4/P_0 - P_2/P_0$  correlation. First, there is again an excess of simulated clusters for large  $x_p$  values; i.e. there is generally too much substructure in the simulated clusters. However, the inconsistency of the distributions in the  $x_p$  direction is much more significant than in the  $P_4/P_0 - P_2/P_0$  case; i.e. KS probability of only 0.15% ( $> 3\sigma$ ) that the simulated and ROSAT clusters are consistent. (Note that this inconsistency involving an “odd moment” differs markedly from the centroid-shift results from Mohr et al. 1995.) In the  $y_p$  direction the distributions are consistent at the same level as before with KS probability  $P(\text{KS})=37\%$ ; i.e. again, individual clusters of similar dynamical ages (position along the evolutionary track) “look” like real clusters in terms of their morphology.

The conclusions from the the  $P_3/P_0 - P_2/P_0$  correlations are not independent of those from the  $P_4/P_0 - P_2/P_0$  correlation because they both involve  $P_2/P_0$ . However, the two sets of correlations give complementary information. The power ratio  $P_3/P_0$  is particularly sensitive to bimodal cluster structure (with clumps separated by  $r_{sep} \lesssim$  the aperture size) where the secondary component is smaller than the primary component ( $P_3/P_0 = 0$  for exactly equal-sized spherical components since the current set of ratios are centered on the centroids of the images – BTa). On the other hand, the even moments are particularly sensitive to the overall ellipticity or “boxiness” of clusters. The ratio  $P_2/P_0$  will be large for highly elongated structures such as flattened single component clusters and bimodals with comparably sized components. The very significant deficit of high  $x_p$  clusters in the  $P_3/P_0 - P_2/P_0$  case indicates that there are far too many bimodal clusters with smaller secondaries in the simulations as compared to the data. The somewhat less significant deficit of large  $x_p$  clusters in the  $P_4/P_0 - P_2/P_0$  case indicates a less numerous surplus in highly elongated single component clusters and equally sized bimodals.

We now consider  $P_1^{(pk)}/P_0^{(pk)}$  which is defined so that the aperture is centered at the peak of  $\Sigma_x$ . By construction  $P_1^{(pk)}/P_0^{(pk)}$  is not independent of the  $P_m/P_0$ , however, it is useful to consider power ratios centered on the peak emission because they are particularly sensitive to bimodal clusters with comparably sized components while being insensitive to ellipsoidal single component clusters. Figure 9 shows the distribution of clusters in  $P_1^{(pk)}/P_0^{(pk)}$ . The surplus of bimodal clusters suggested by the  $P_4/P_0 - P_2/P_0$  results is confirmed again by the excess in large  $P_1^{(pk)}/P_0^{(pk)}$  simulated clusters. The KS probability for consistency is  $P(\text{KS})=1.2\%$  when all observed clusters

are considered. This result disagrees with the centroid-shift results of Mohr et. al. (1995).

### 3.3. Statistical Considerations for Higher Redshift ( $z > 0.1$ )

At present, there is a paucity of X-ray data available for high-redshift ( $z \gtrsim 0.2$ ) clusters (e.g., Donahue & Stocke 1995, Castander et al. 1994). Unfortunately, this situation will persist until the launch of AXAF which will finally enable higher redshifts to be significantly probed. However, comparison of high redshift simulated clusters with both the observed ROSAT sample and low redshift simulated clusters allows the study of cluster evolution in the  $\Omega = 1$  CDM cosmogony. A principle consideration is how the cluster formation rate (i.e.  $x_p$  distribution – see beginning of §3.2.) varies with redshift and whether the results show the strong evolution expected from analytic studies (e.g., Richstone et. al. 1992). We also suggest potential observational tests of the CDM cosmogony with high  $z$  clusters.

The  $z > 0.1$  simulated clusters can be treated in the same manner as the low redshift clusters. Each cluster is viewed down three random, orthogonal axes and the power ratios are plotted in the manner of Figures 4 and 5. This method of generating the sample of high redshift simulated clusters is not entirely consistent since we are considering the same clusters at high and low redshift. We might expect that since individual clusters evolve in different ways, the sample that should be compared with observations will not consist of the same clusters at different redshifts. As with the incompleteness of the simulated sample discussed in the previous section, we cannot usefully address this issue at present and thus our following analysis is intended only to be suggestive.

The location of clusters can be expressed in terms of the rotated coordinates  $(x_p, y_p)$  where we assume the same set of coordinates used in the low  $z$  cases in order to have consistent comparisons. The distribution of clusters in the  $P_4/P_0 - P_2/P_0$  plane are shown in Figure 10 and the distribution in  $P_3/P_0 - P_2/P_0$  are shown in Figure 11. Three redshift ranges are considered. The range  $z_1$  consists of simulated clusters at  $z = 0.14$  and  $0.23$ , the range  $z_2$  is composed of clusters at  $z = 0.35$  and  $0.49$ , and the range  $z_3$  is given by the clusters at  $z = 0.68$ . Higher redshifts are not considered because some of the six NFW clusters begin to disperse by  $z > 0.68$ .

Consider first the  $P_4/P_0 - P_2/P_0$  plane. Similar to what we found for the low-redshift simulated clusters (see §3.2.), the high-redshift simulated clusters are roughly evenly distributed in the  $x_p$  direction with a sizeable number of large  $x_p$  clusters. KS tests of the consistency of low and high redshift simulations yield  $P(\text{KS}:z_1, z_{low}) = 83\%$ ,  $P(\text{KS}:z_2, z_{low}) = 35\%$ , and  $P(\text{KS}:z_3, z_{low}) = 15\%$ . This indicates that the intermediate  $z$  simulated clusters  $z_1$  and  $z_2$  have  $x_p$  distributions consistent with that of  $z_{low}$ , while  $z_3$  is in marginal disagreement. These relationships are further supported by comparing the high-redshift simulated clusters with the observed ROSAT clusters which are all at low  $z$ :  $P(\text{KS}:z_1, \text{data})=4.9\%$ ,  $P(\text{KS}:z_2, \text{data})=12\%$ , and  $P(\text{KS}:z_3, \text{data})=0.55\%$ .

(Again, the highest redshift clusters seem to have somewhat different properties from the low redshift simulated clusters.) The distribution of high redshift simulated clusters in the  $y_p$  direction is consistent with the data, except again for the highest redshift case.

These results demonstrate that the morphologies of the sample of simulated clusters, as measured by the even power ratios, remains essentially unchanged over the redshift range from the present to  $z \sim 0.6$ . The equivalence of the  $x_p$  distributions means that by  $z \sim 0.6$  the rate of clusters arriving in the upper regions of the evolutionary track has come into balance with the relaxation rate. If we assume that the relaxation rate does not depend strongly on the cosmological model or on the epoch being considered (i.e., the self gravity of cluster material dominates both tidal forces from surrounding large-scale structures and the effects of an expanding universe), the formation rate of clusters must then be constant.

Whether this balance between formation and relaxation after a specific redshift is a common feature of cluster formation scenarios or instead depends on the specific cosmogony requires consideration of a variety of models. However, this result is not clearly anticipated by semi-analytic considerations of structure formation such as those by Richstone et al. (1992). The constancy in the distribution of cluster morphologies and the apparent change at  $z \sim 0.6$  provides a new test of the model. Current X-ray observations are beginning to probe this redshift range, but the usefulness of the data is limited by poor photon statistics and by the difficulty of identifying clusters at these redshifts. Hopefully future high resolution observations by AXAF will sample this regime with some completeness.

If correct, the change in the distribution of power-ratios at  $z \gtrsim 0.6$  is of interest. At low redshifts, clusters are distributed evenly in  $y_p$  about the best fit line to the data. The  $z_3$  clusters, however, are strongly skewed so that many more have positive values of  $y_p$ . These clusters sit above the correlation line in Figure 6 and would be considered relatively unrelaxed with significant small-scale structure. This is supported by the the distribution along the  $x_p$  direction which shows an excess of clusters with very large values of  $x_p$ . These properties identify  $z \gtrsim 0.6$  as an epoch where clusters are rapidly forming out of background matter and where the relaxation rate is insufficient to balance the formation rate. The formation rate levels off in the epochs immediately after this time.

The cluster distributions in the  $P_3/P_0 - P_2/P_0$  are consistent with the above behavior although with somewhat more uncertainty. The  $z_3$  clusters are again skewed toward high  $x_p$  values relative to those at lower redshifts and the distribution in  $y_p$  indicates an overpopulation at positive  $y_p$ . The time around  $z \sim 0.6$  is also identified as the era of rapid cluster formation. Clusters at  $z_1$ , however, also show a shift to large  $y_p$ , although it is less significant than at high redshift and the shift is into the bin just adjacent to  $y_p = 0$ . This may be the result of a statistical fluctuation since there are  $\sim 36$  measurements of the power ratios at  $z_1$ . We could have just picked a particular time which happens to give a  $\lesssim 2\sigma$  fluctuation to larger  $y_p$ . Alternatively, the number of clusters with large  $P_3/P_0$  could really be high at certain redshifts. This issue cannot be settled



with the present limited simulations.

The distribution of  $P_1^{(pk)}/P_0^{(pk)}$  for the higher redshifts is plotted in Figure 12. For the  $z_1$  and  $z_2$  clusters, the results are consistent with those from the other power ratios. However, the distribution shifts towards *smaller*  $P_1^{(pk)}/P_0^{(pk)}$  at the highest redshifts considered. At first, this may appear to contradict the picture of cluster evolution outlined above, but it actually provides an interesting additional constraint while highlighting the utility of the dipole power ratio. Recall that  $P_1^{(pk)}/P_0^{(pk)}$  is large for bimodal clusters with roughly equally sized components but small for elongated single component clusters. In contrast, the centroided even power ratios are large for both sets of clusters (BTa). The small number of large  $P_1^{(pk)}/P_0^{(pk)}$  clusters at high  $z$  and the excess of positive  $y_p$  clusters in the  $P_4/P_0 - P_2/P_0$  plane implies that there are many rather unrelaxed single component clusters, but very few large bimodal clusters; here “single component” means an isolated but possibly morphologically complex lump of material. This is a reasonable situation. At the earliest times, single lumps are forming out of the background matter distribution. These are unrelaxed so have large centroided power ratios; the distribution is skewed towards high  $x_p$  and positive  $y_p$ . However, the bimodals can only occur after two of these nascent lumps have collided and begun to merge. This occurs some time after the initial formation of the single lumps. Thus, the epoch around  $z \sim 0.6$  is a the period when virializing single component clusters are rapidly emerging from the background matter. After this time, clusters form primarily by mergers with other lumps (there are few single lumps emerging from the background since the distribution in  $y_p$  is evenly spread between positive and negative values) and it is this rate which balances the rate of relaxation and results in the constant distribution of clusters along the  $x_p$  direction of the power ratio correlations. It is evident that the cluster formation rate is not simply the rate of making bound mass concentrations out of initial density fluctuations, but also involves knowing the merger rate at the given time.

### 3.4. Constraints on Cluster Parameters from the Evolutionary Track

In the  $z$  projection the CL1 cluster evolves very nearly along a line in the  $P_4/P_0 - P_2/P_0$  plane with a slope that agrees well with that of the best-fit line to the ROSAT data. We consider simple parametrized models of the simulated cluster in order to understand how the cluster adjusts its morphology to follow the evolutionary track displayed by the ROSAT clusters. At early times, the two components of the bimodal cluster are well separated so can be considered individual clusters for the present purposes. The surface brightness profile of each component is fitted to the  $\beta$  model (eq. 7) assuming circular isophotes  $\epsilon_x = 0$ . At later times ( $z \lesssim 0.49$  – panel (f) of Figure 3) the merged remnant resembles a rather high ellipticity  $\beta$  model and is consequently fitted with finite  $\epsilon_x$ .

Table 1 gives the best fit parameters at various redshifts. Consider first the bimodal cluster at  $z = 0.95$  and 0.68. The top component (the uppermost clump in Figure 3) evolves little with both

$\beta$  and  $a_{core}$  retaining steady and realistic (e.g., Jones & Forman 1984) values. The central clump has a constant  $a_{core}$  but a surface brightness profile which becomes shallower in time. This simple modification to the naive view that a bimodal cluster evolves only due to the mutual approach of its two unchanging components allows the line followed by the cluster in power ratio space to agree with observations. Specifically, the path indicated by the open stars of Figure 6 is modified, for example, by allowing  $\beta$  for one of the clumps to decrease with time, so that it becomes shallower, in agreement with the distribution of observed clusters. An interesting aspect of this result is that the rate at which  $\beta$  changes must be accurately tuned, in concert with the approach speed of the two clumps, so that the corresponding path followed in power ratio space is correct. The rate of evolution of  $\beta$  likely depends primarily on the actions of self gravity in the given subclump. However, the rate of approach of the subclumps may be controlled or at least influenced by the large scale matter distribution, tidal fields, or the underlying cosmological model. Thus the slope of the correlation line potentially gives information both on the rate of gravitational relaxation and on cosmology, but it will require further simulations to disentangle the various dependences.

A further consequence of the above parameter evolution is that simulations of cluster mergers are only realistic if the approach speed of the two clumps is correctly chosen so that the cluster satisfies the above evolutionary track constraint. Subclumps cannot approach each other at arbitrary speeds, otherwise they will evolve into a region of power ratio space where no clusters are observed to reside. This new restriction is important for many issues which are addressed by simulations. For example, simulations based on cosmologically motivated initial conditions show that cluster gas relaxes to hydrostatic equilibrium on relatively short time scales (e.g., Tsai, Katz, & Bertschinger 1994, NFW). In contrast, some simulations concentrating on the study of specific mergers indicate that relaxation could take much longer (e.g., Roettiger, Burns, & Loken 1993; Nakamura et al. 1995). However, the subclumps in these studies are allowed to merge at rather high speeds (a few times the sound speed). It is not clear that the clusters in these simulations would obey the observational constraints described here and thus whether they represent realistic cluster simulations.

The evolutionary track also places constraints on the evolution of single-component clusters. The simulated cluster at  $z = 0.49$  and  $0.35$  are fit to single  $\beta$  models. (At  $z = 0.49$ , two defined emission peaks remain, however, the separation is very small  $r_{sep} \sim 300$  kpc so our single cluster assumption is adequate for the present purposes.) Table 1 shows that the evolution in this case consists of the surface brightness profile becoming both shallower and more centrally concentrated. This modification to the naive view that single clusters evolve simply by becoming rounder is again sufficient to ensure that the cluster follows the required path in power ratio space. As before, gravitational relaxation likely leads to the required parameter evolution of the cluster, however, external tidal fields could also play a role.

#### 4. Comparison of Dark Matter and Gas

An important assumption underlying our analysis is that the X-ray emission traces the underlying mass sufficiently well to allow the power ratios to quantify the evolutionary state of the underlying mass. Although we expect the distributions to be different in detail even in rather virialized clusters (e.g, Buote & Canizares 1996 and references therein), a simple qualitative examination of the simulated clusters shows that the gross morphological characteristics of the dark matter and of the gas are similar (e.g., Buote & Tsai 1995b; NFW). The power ratios allow this connection to be quantified in detail. As an example, Figure 13 shows the power ratios computed on a 1 Mpc aperture for the dark matter distribution of the largest cluster CL1. Specifically,  $\Sigma \equiv \int \rho_{DM} dz$  is used in eqs. (2) and (3) where  $\rho_{DM}$  is the dark matter mass density. The expansion of eq. (1) in this case will give exactly the projected potential.

The cluster dark matter is distributed much like the gas shown in Figures 1, 2, and 3 (see also NFW). Concentrations of dark matter coincide with concentrations of gas and the correspondence is retained in the subsequent mergers and evolution of the clumps. However, after mergers, the distributions of the gas and dark matter differ in that the dark matter retains a larger quadrupole moment than does the gas. In fact, gas distributed in hydrostatic equilibrium under the influence of an ellipsoidal dark matter halo is rounder than the underlying mass distribution (Buote & Canizares 1996; Buote & Tsai 1995b). Thus an exact numerical correspondence between the power ratios for the gas and the dark matter is not expected. The dark matter power ratios will in general be larger both because it dominates the mass, hence is less “round” than the gas, and because it evolves less rapidly since non-axisymmetric structures are not erased as readily as in the dissipational gas. What is important, however, is that the gas and the dark matter give a consistent picture of the state of the cluster.

The figures show that the dark matter power ratios evolve generally like those of the gas, although the values extend over a smaller region of the space, as we expect. At early times, the two clumps which form the nascent cluster are widely separated. As they approach and merge, the power ratios move down and to the left, although the values remain large compared to that of the gas. However, the notion of the evolutionary track is clearly valid for the dark matter and the dynamical states as classified by the dark matter and gas are consistent. Note, however, that the track for the dark matter does not seem to coincide with that of the gas. For example, the track in the  $P_4/P_0$ – $P_2/P_0$  correlation falls below that of the gas at some redshifts. There is no *a priori* reason that the two tracks should be exactly the same; rather this serves to illustrate that the different aspects of the evolution of the dark matter and gas may be usefully quantified and analyzed by the power ratios. Detailed statistical analyses should provide interesting information on the relative behaviors of dark matter and gas as they evolve simultaneously in the CDM model which has, among others, implications for dynamical estimates of the mass distributions of galaxy clusters using X-rays. These issues are beyond the scope of the present paper and will be considered elsewhere.

## 5. Discussion and Conclusions

With the aid of hydrodynamical simulations of cluster formation, we have further demonstrated the utility of the power ratios for quantifying the morphology and evolution of galaxy clusters and have shown their promise for providing new constraints on cosmology. These statistics are dynamically motivated: each power ratio measures the square of a higher order moment of the projected potential relative to the monopole term and hence quantifies the amount of higher order, non-axisymmetric (for odd moments) structure present in the projected potential. The power ratios were computed elsewhere for a sample of low redshift ( $z \lesssim 0.2$ ) clusters observed by ROSAT (BTb) and displayed interesting correlations. The observed clusters occupy only a restricted region of the space defined by the three lowest order power ratios ( $\log P_2/P_0$ ,  $\log P_3/P_0$ ,  $\log P_4/P_0$ ), extending in a thick straight filament outward from the origin. This filament, or any of the correlation lines resulting from projection of the filament onto the coordinate planes, was interpreted in the context of bottom-up cluster formation scenarios as the evolutionary track followed by clusters as they form out of the background distribution (moving onto the track from above), relax (moving down along the track towards the origin), or merge with a clump previously outside the given aperture (moving outward from the origin along the track).

The cluster simulations confirm the above picture of the evolutionary track and show that clusters formed in the standard  $\Omega = 1$  CDM cosmogony evolve along the same track as given by the data. In addition, a combination of the simulations and simplified parametric cluster models allow an intuitive understanding of cluster evolution. A bimodal cluster, for example, would evolve by the mutual approach of the two components. A simple model consisting of two unchanging components (taken to be  $\beta$  models) approaching each other follows a straight line in power ratio space that mimics the qualitative aspects of the evolutionary track, but has a steeper slope. The simulations show that if in addition the components evolve individually by self gravity giving smaller core radii or shallower mass distributions, the slope will agree with that of the observed track. Since the evolution of the components is likely driven mainly by self gravity, the rate of approach of the two clumps must be finely tuned so as to ensure that the cluster moves in an allowed (i.e. probable) region of power ratio space. This approach speed may depend upon the assumed cosmology. Hence the slope of the evolutionary track may constrain the underlying cosmology. A large suite of simulations with many different cosmogonies must be examined to disentangle the various dependences.

BTb asserted that the distribution of ROSAT clusters along the evolutionary track is a measure of the balance of the formation and relaxation rates of clusters. Guided by the success of the evolutionary track interpretation shown by the simulated clusters, in this paper we explicitly defined these rates in terms of the evolutionary track. We considered the “relaxation rate” to be the hypothetical rate at which clusters would move down the evolutionary track in isolation; i.e. when undisturbed by mass accreting from outside the specified aperture. We defined the “formation rate” to consist of a “birth rate” and “merger rate”. The birth rate is the rate at

which clusters first appear on the upper parts of the track immediately after forming out of the background matter while the “merger rate” is the rate at which a mature cluster jumps from a lower position to a higher position on the track due to the accretion of mass from outside the specified aperture. Provided these rates have physical meanings similar to conventional definitions, then this would suggest that to probe  $\Omega$  effectively we should consider the location of clusters in power-ratio space relative to a set of rotated coordinates where one axis lies along the correlation line.

We compared the distribution of simulated clusters along and perpendicular to the evolutionary track with the observed distributions of ROSAT clusters. It was therefore useful to consider a rotated coordinate system  $(x_p, y_p)$  where  $x_p$  coincided with the evolutionary track and  $y_p$  was taken to be perpendicular to it. The simulated cluster sample at low redshift contained too many large  $x_p$  clusters relative to the observations. Provided that our assumptions regarding the construction of the simulated cluster sample are not grossly inaccurate (e.g., that each simulated cluster represents the “average” cluster of that size) then the  $\Omega = 1$  cosmogony produces too many clusters with significant substructure. This latter conclusion is supported by ongoing work on dissipationless simulations where the simulated clusters sample is much more statistically significant (Buote & Xu 1996). Note these conclusions differ from previous studies (e.g., Mohr et al. 1995; Jing et al. 1995).

Since the distribution in the  $x_p$  direction results from the combined actions of formation and relaxation, either the formation rate of clusters in the simulations is too high, or the relaxation rate is too low. Since relaxation is treated self-consistently, it is likely that the formation rate with  $\Omega = 1$  is too high.  $\Omega < 1$  cosmogonies are thus preferred, given the arguments of Richstone et al. (1992), and agrees with results from recent cluster dynamical studies (e.g., Carlberg et al. 1995), over-density of baryons in clusters (e.g., White et al. 1993; Buote & Canizares 1996), and galactic disk arguments (Toth & Ostriker 1992), but does not agree with analytic treatments of cluster collapse (e.g., Richstone et al. 1992; Lacey & Cole 1993). Part of this latter disparity may result from the use of qualitative estimates of the fraction of clusters possessing substructure in place of quantitative statistics employed in the present study and because of the reliance on linear theory results. The application of power ratios to analytic treatments of cluster collapse may clarify the reasons for the above disagreement as well as elaborating on the  $\Omega$  dependence of cluster evolution. These arguments will be presented elsewhere. It will in any case also be useful to confirm the present results with more statistically complete samples of simulated clusters. This necessarily implies that we consider purely dissipationless dark matter simulations where the computational demands are tractable (Buote & Xu 1996).

The distributions of the simulated and observed ROSAT clusters agree in the  $y_p$  direction; i.e. perpendicular to the evolutionary track. For a given point on the evolutionary track a cluster lying perpendicularly to the left (i.e. positive  $y_p$ ) of the track possesses a larger amount of smaller scale structures (i.e. excess  $P_3/P_0$  or  $P_4/P_0$ ) but a less pronounced aggregate, larger scale structure (i.e. less  $P_2/P_0$ ); the opposite is true for clusters lying perpendicularly to the right (i.e. negative

$y_p$ ) of the track. Intuitively the agreement of the ROSAT and simulated cluster distributions in  $y_p$  implies that for a particular dynamical age (i.e. at a particular position along the evolutionary track) simulated clusters in the  $\Omega = 1$  simulation tend to “look” like real clusters. Unlike the cluster distributions in the  $x_p$  direction, the physical implications of this are unclear at present. One possibility is that the shape of the power spectrum of initial perturbations has been correctly chosen for the simulations so as to give the observed distribution of structure on various scales inside the cluster. Alternatively, the observed distribution may be simply a general feature of gravitational relaxation. We cannot determine which of the two possibilities is more likely without recourse to simulations with a variety of power spectra (Buote & Xu 1996). However, the study of this interesting aspect of cluster evolution has become possible with the power ratios.

We examined how cluster evolution in the CDM model changes with time and suggested corresponding observational tests of the model. We found that the distributions of simulated clusters in both the  $x_p$  and  $y_p$  directions are essentially constant from the present up until a redshift of  $\sim 0.6$ . We caution that this result may be uncertain due both to the small number of simulated clusters and because the selection criterion for the clusters at high redshifts was not entirely consistent with that of the observed sample of clusters. However, if the above results hold, then, when coupled with the assumption that the relaxation rate is nearly constant with redshift, the formation rate (i.e. birth rate + merger rate, as above), is constant over the indicated period of time.

At  $z \gtrsim 0.6$  the clusters in the simulations primarily consist of single unrelaxed concentrations of mass. At later times, however, cluster evolution is dominated by the merger of nearly equal-sized clumps, as previously indicated by other studies (e.g. Lacey & Cole 1993). Then at early times clusters consist of single lumps of gas and dark matter forming out of the background distribution. At  $z \sim 0.6$ , the merger of the nascent clumps becomes the dominant means of cluster growth. The rate of mergers appears basically constant from that time onwards to the present – a result unanticipated by analytic studies of cluster evolution (e.g., Richstone et al. 1992). Whether the constancy in the merger rate (as defined by the power ratios) is a general feature of hierarchical clustering models, or if the redshift at which mergers begin to dominate cluster evolution changes with model parameters, awaits further study. However, the above results suggest that the era around  $z \sim 0.6$  may have observationally interesting properties which can be considered with the expected high quality data from AXAF.

We are grateful to J. F. Navarro for graciously allowing us to use his cluster simulations as the basis of this paper. DAB acknowledges the hospitality of CITA during the final stages of this work.

Table 1: Cluster Parameters

$z$	Clump	$r_{sep}$ (kpc)	$\beta$	$a_{core}$ (kpc)
0.95	top	1230.	0.852	92.1
0.95	central	1230.	0.938	110.
0.68	top	1050.	0.844	94.8
0.68	central	1050.	0.839	104.
0.49	central	–	1.34	629.
0.35	central	–	0.864	325.

---

Note. — The best fit  $\beta$  model parameters are given for various clusters and cluster components. The second column indicates either the top or central component of the bimodal cluster in Figure 3 or the central cluster after  $z = 0.49$ . The third column gives the separation of the cluster components.

## REFERENCES

- Bartelmann, M., Ehlers, J., & Schneider, P. 1993, *A&A*, 280, 351
- Briel, U. G., & Henry, J. P. 1993, *A&A*, 278, 379
- Buote, D. A., & Canizares, C. R. 1996, *ApJ*, 457, 565
- Buote, D. A., & Tsai, J. C. 1995a, *ApJ*, 452, 522 (BTa)
- Buote, D. A., & Tsai, J. C. 1995b, *ApJ*, 439, 29
- Buote, D. A., & Tsai, J. C. 1996, *ApJ*, 458, 27 (BTb)
- Buote, D. A., & Xu, G. H. 1996, in preparation
- Castander, F. J., Ellis, R. S., Frenk, C. S., Dressler, A., & Gunn, J. E. 1994, *ApJ*, 424, L79
- Carlberg, R., Yee, H. K. C., Ellingson, E., Abraham, R., Gravel, P., Morris, S., & Pritchett, C. J. 1995, preprint
- Cavaliere, A., & Fusco-Femiano, R. 1976, *A&A*, 49, 137
- Donahue, M., & Stocke, J. T. 1995, *ApJ*, 449, 554
- Dressler, A. & Shectman, S. A. 1988, *AJ*, 94, 985
- Edge, A. C., Stewart, G. C., Fabian, A. C., & Arnaud, K. A. 1990, *MNRAS*, 245, 559
- Evrard, A. E., Mohr, J. J., Fabricant, D. G., & Geller, M. J. 1993, *ApJ*, 419, 9
- Geller, M. J., & Beers, T. C. 1982, *PASP*, 94, 421
- Jing, Y. P., Mo, H. J., Börner, G., & Fang, L. Z. 1995, *MNRAS*, in press
- Jones, C., & Forman, W. 1984, *ApJ*, 276, 38
- Kaiser, N., & Squires, G. 1993, *ApJ*, 404, 441
- Kauffmann, G., & White, S. D. M. 1993, *MNRAS*, 261, 921
- Lacey, C., & Cole, S. 1993, *MNRAS*, 262, 627
- Mohr, J. J., Fabricant, D. G., & Geller, M. J. 1993, *ApJ*, 413, 492
- Mohr, J. J., Evrard, A. E., Fabricant, D. G., & Geller, M. J. 1995, *ApJ*, 447, 8
- Nakamura, F. E., Hattori, M., & Mineshige, S. 1995, *A&A*, in press
- Navarro, J. F., Frenk, C. S., & White, S. D. M. 1995, *MNRAS*, 275, 720 (NFW)
- Pfeffermann, E. et al. 1987, *Proc. SPIE*, 733, 519
- Roettiger, Burns, & Loken 1993, *ApJ*, 407, L53
- Richstone, D. O., Loeb, A., & Turner, E. L. 1992, *ApJ*, 393, 477
- Squires, G., Kaiser, N., Babul, A., Fahlman, G., Woods, D., Neumann, D. M., & Böhringer, H. 1995, *ApJ*, submitted



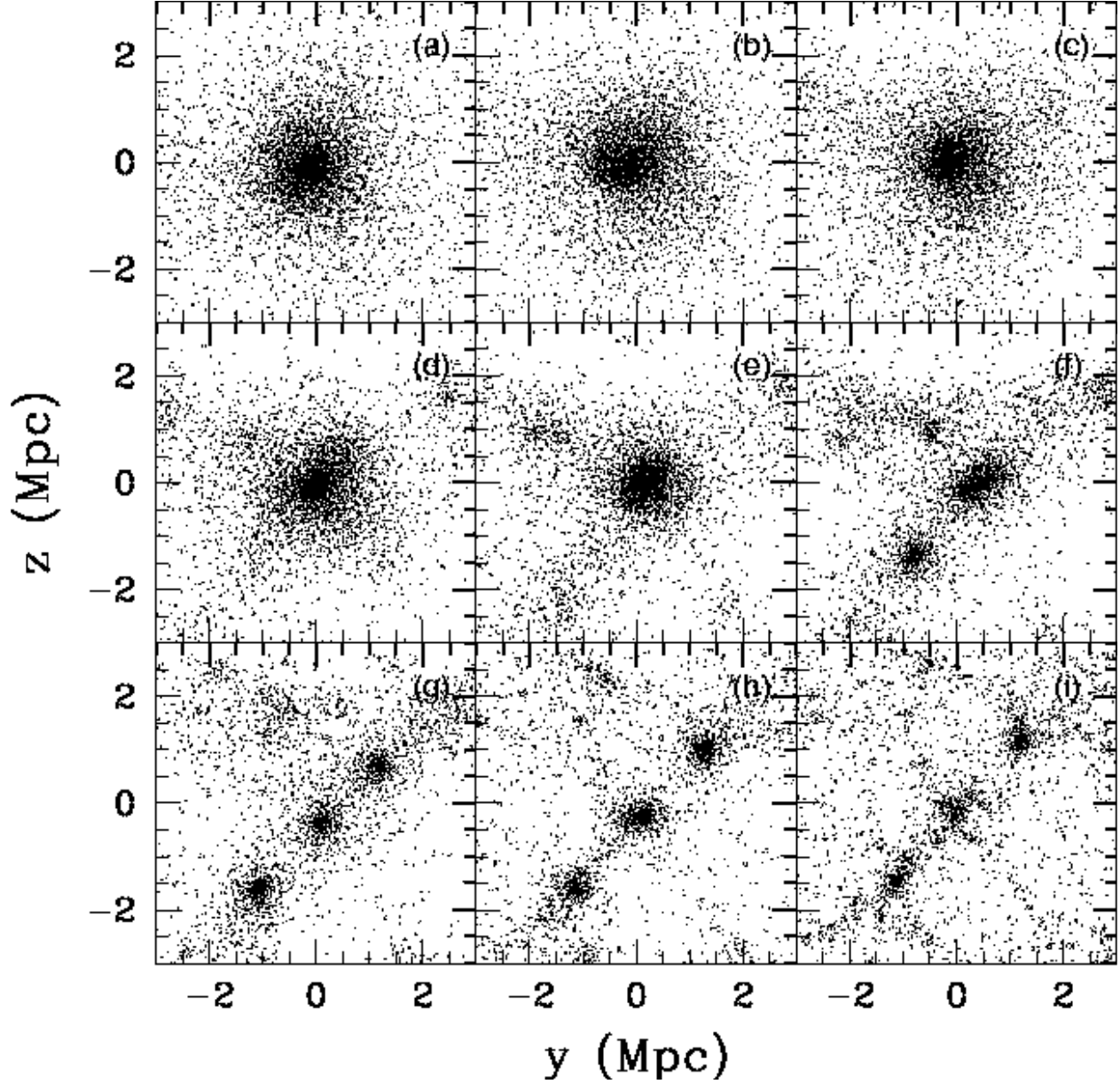
Toth, G., & Ostriker, J. P. 1992, *ApJ*, 389, 5

Tsai, J. C., Katz, N., & Bertschinger, E. 1994, *ApJ*, 423, 553

West, M. J., & Bothun, G. D. 1990, *ApJ*, 350, 36

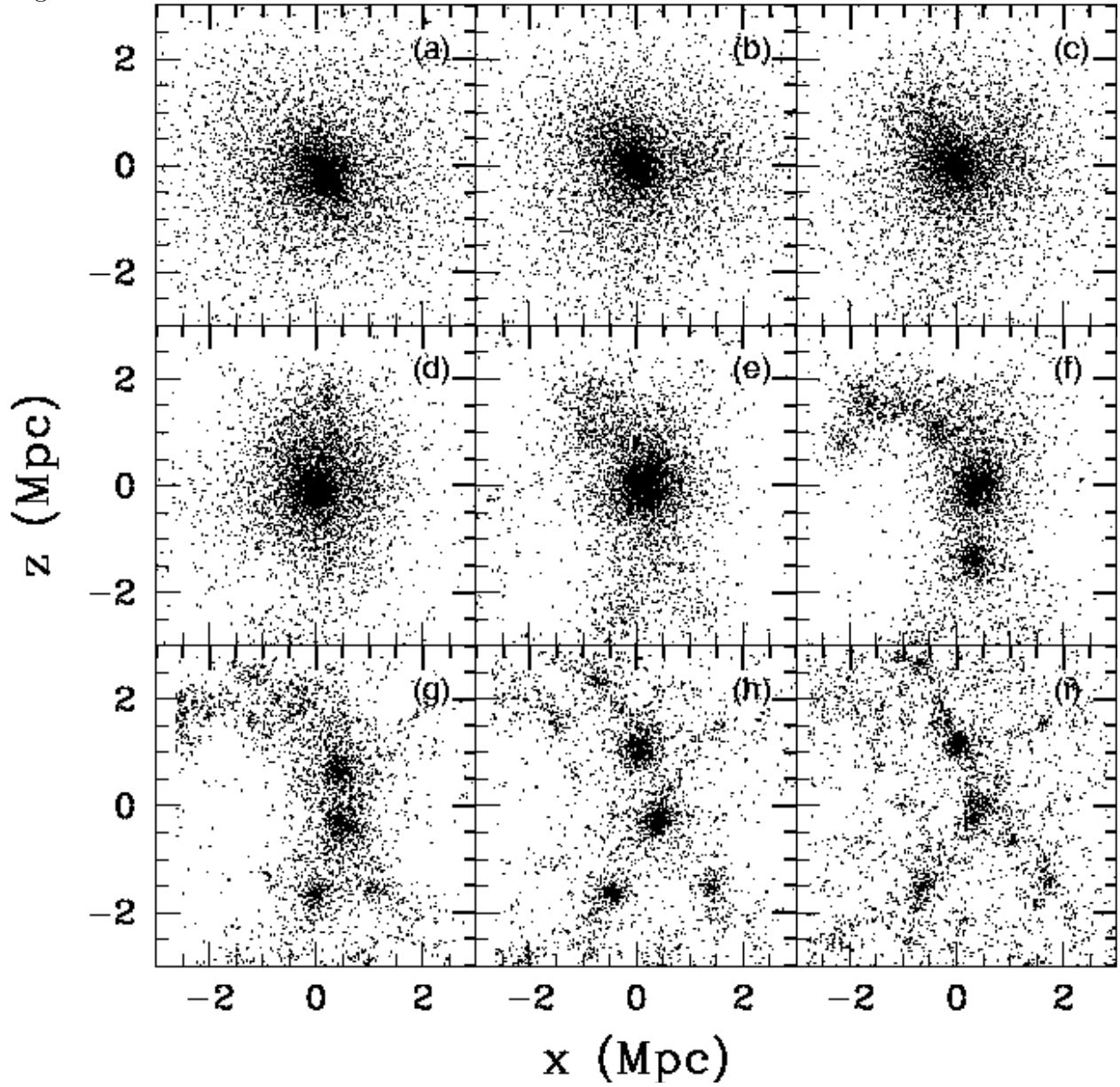
White, S. D. M., Navarro, J. F., Evrard, A. E., & Frenk, C. S. 1993, *Nature*, 366, 429

Fig. 1.—



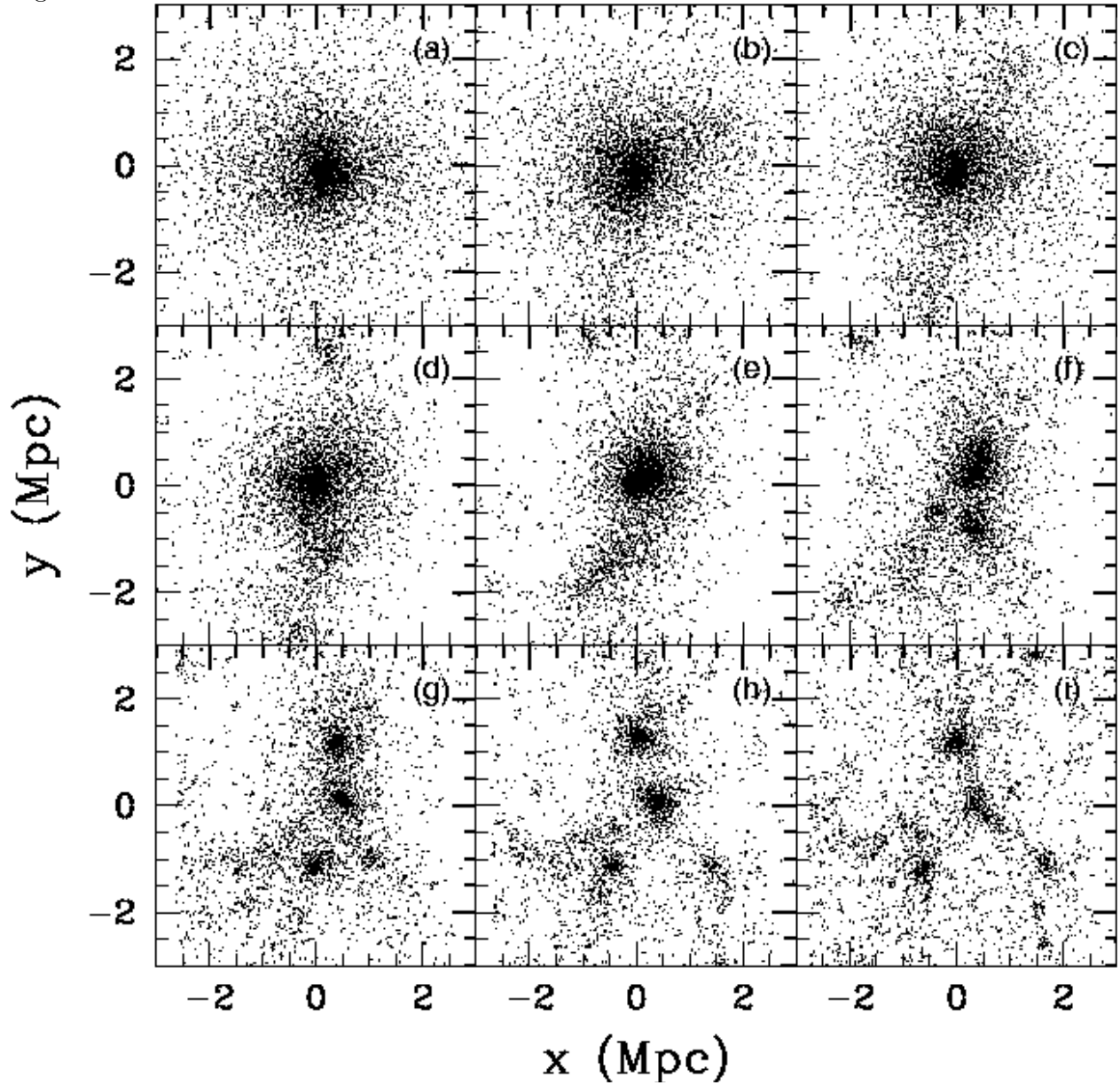
The SPH gas particles in the largest simulated cluster of Navarro et al. (1995; cluster CL1) are shown when viewed down the  $x$  axis. Distances are given in physical units of Mpc. Each panel corresponds to a different redshift: (a) gives  $z = 0$  (the present), (b) gives  $z = 0.065$ , (c) gives  $z = 0.14$ , (d) gives  $z = 0.23$ , (e) gives  $z = 0.35$ , (f) gives  $z = 0.49$ , (g) gives  $z = 0.68$ , (h) gives  $z = 0.95$ , and (i) gives  $z = 1.4$ .

Fig. 2.—



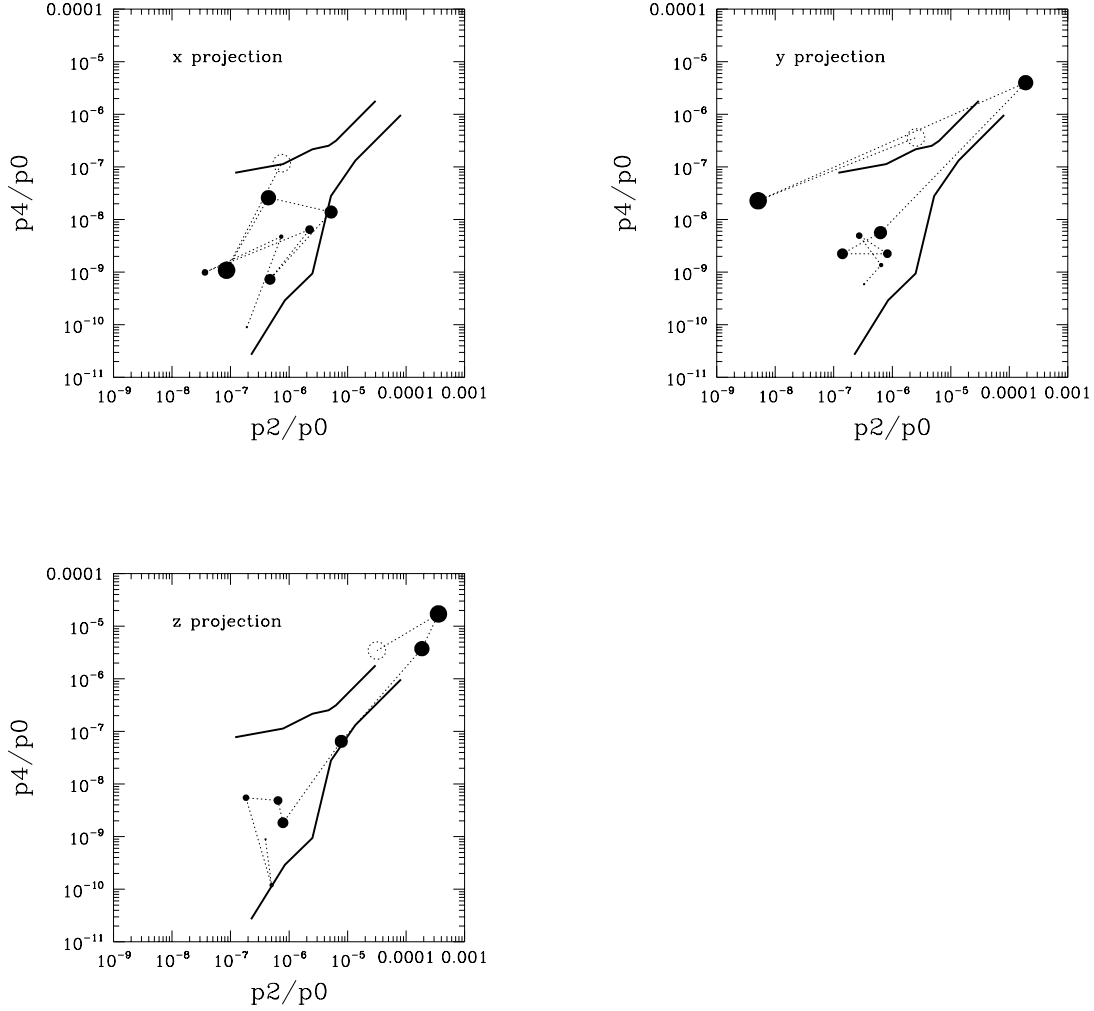
The SPH gas particles for cluster CL1 are shown viewed down the  $y$  axis for the same set of redshifts as Figure 1.

Fig. 3.—



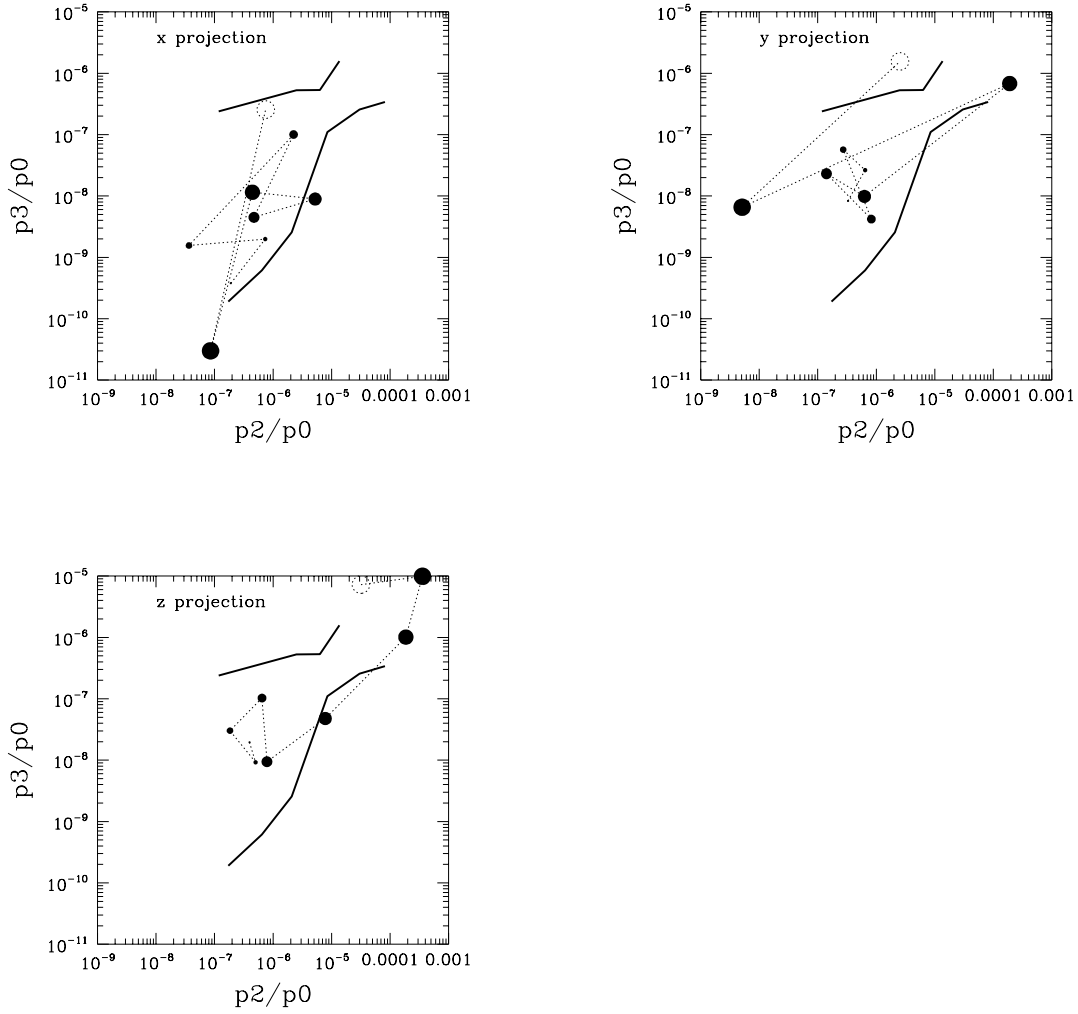
The SPH gas particles for cluster CL1 are shown viewed down the  $z$  axis for the same set of redshifts as Figure 1.

Fig. 4.—



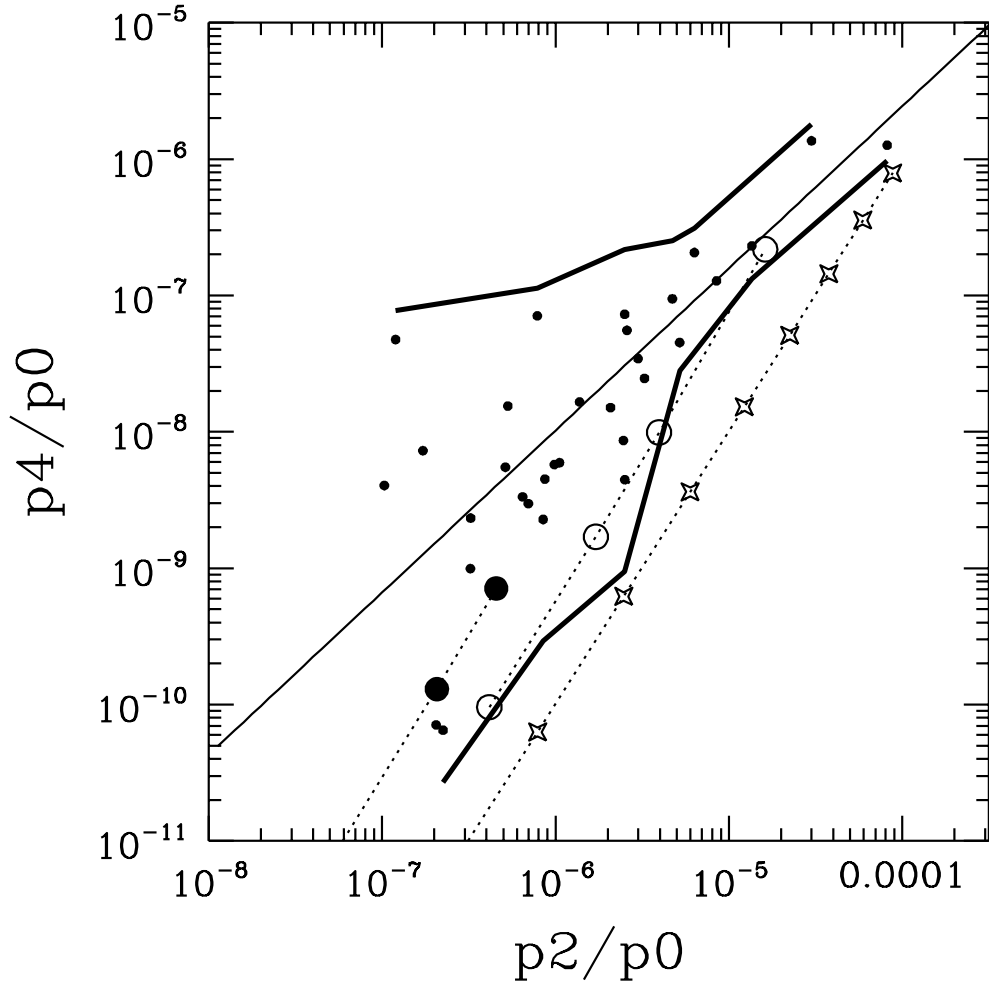
The locations of the largest cluster (CL1) in the plane formed by  $P_4/P_0$  and  $P_2/P_0$  are given for, (a) the  $x$  projection, (b) the  $y$  projection, and (c) the  $z$  projection. An aperture of 1 Mpc is assumed. The dashed empty circle corresponds to the earliest redshift,  $z = 1.4$ . The filled circles show smaller redshifts where the size of the circle decreases with redshift. In decreasing size, the circles correspond to  $z=0.95, 0.68, 0.49, 0.35, 0.23, 0.14, 0.065,$  and  $0$ . The circles are connected by a dashed line to emphasize the motion of the cluster in power ratio space. The heavy solid lines indicate approximately the region occupied by the observed power ratios from BTb.

Fig. 5.—



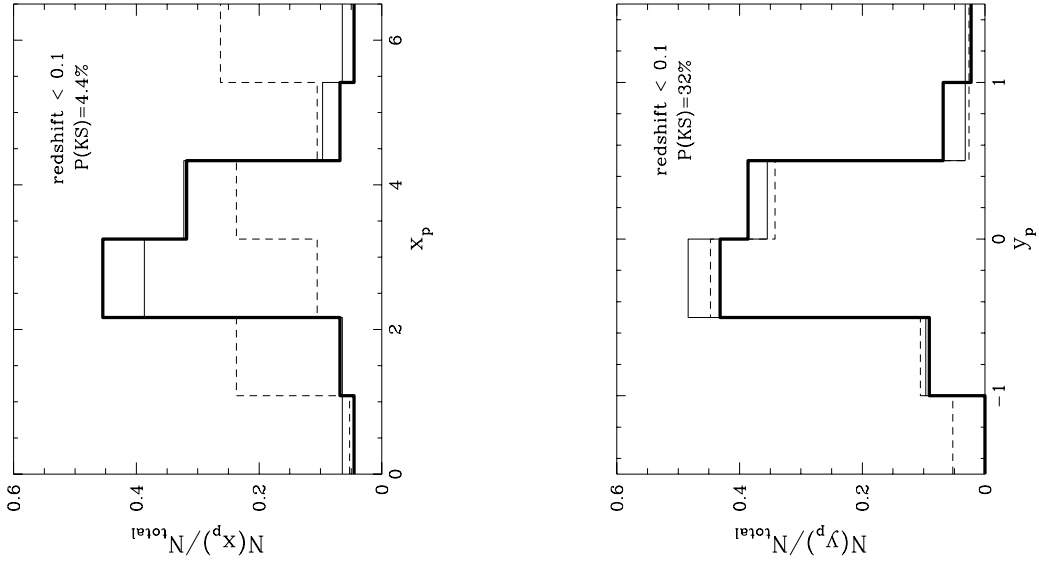
The locations of the largest cluster (CL1) in the plane formed by  $P_3/P_0$  and  $P_2/P_0$  are given for, (a) the  $x$  projection, (b) the  $y$  projection, and (c) the  $z$  projection. The points are plotted as in Figure 4. The heavy solid lines again shows the approximate region occupied by observed values from BTb.

Fig. 6.—



The power ratios  $P_4/P_0$  are plotted versus  $P_2/P_0$ . The small filled circles correspond to the “best measured” clusters in the sample of BTb. The heavy solid lines correspond roughly to the range of observed values and the light solid line is the best fit line to the cluster data. The large open circles are the power ratios computed for single component  $\beta$  models with fixed core radius  $a_{core} = 0.3$  Mpc and  $\beta = 0.75$ . The topmost open circle corresponds to an ellipticity of  $\epsilon_x = 0.6$ . Proceeding downwards, the circles correspond to  $\epsilon_x = 0.3, 0.2$ , and  $0.1$ , respectively. The large filled circles correspond to single  $\beta$  models with  $\beta = 0.75$ ,  $a_{core} = 0.1$  Mpc. The topmost circle has  $\epsilon_x = 0.3$ , and the bottom one has  $\epsilon_x = 0.2$ . The stars give the power ratios for bimodal clusters where each component is a single  $\beta$  model with  $\beta = 0.75$  and  $a_{core} = 0.3$  Mpc. The assumed separation of the components is  $a_{sep} = 1$  Mpc for the topmost star and  $r_{sep} = 0.9, 0.8, 0.7$ , etc. for successively lower stars. Circles and stars are joined with dotted lines to indicate the implied linear relation of  $P_4/P_0$  to  $P_2/P_0$ .

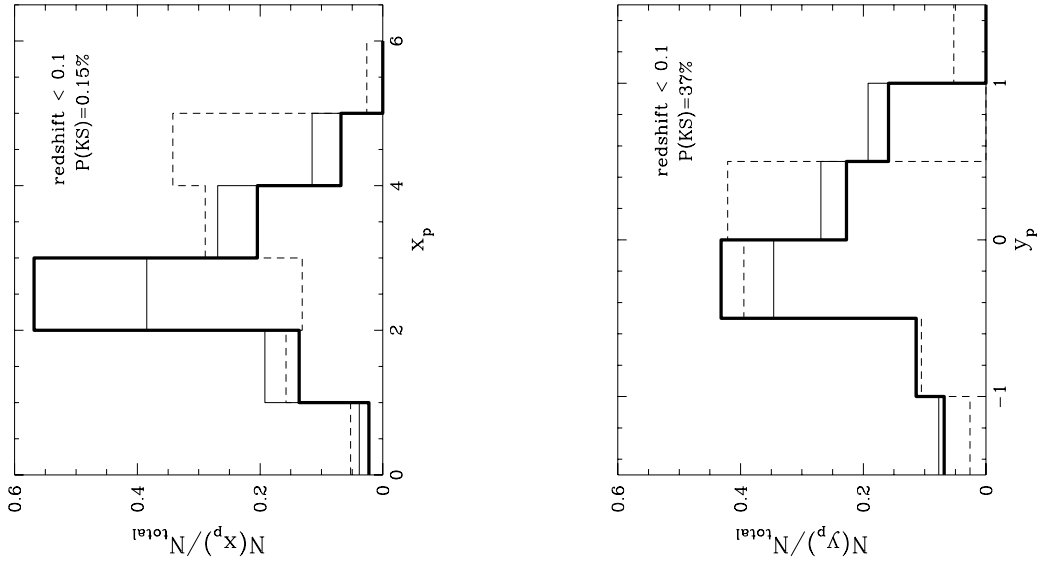
Fig. 7.—



The distribution of clusters in the  $P_4/P_0 - P_2/P_0$  plane are shown. Panel (a) shows the number (normalized to the total number of clusters in the given sample) of clusters with given  $x_p$  (defined in the text). Panel (b) shows the number (normalized to the total) with given values of  $y_p$ . The heavy solid histogram corresponds to the complete observed sample of 44 clusters and the light histogram refer only to the “best measured” cases, numbering 31 clusters. The dashed histogram is the distribution of simulated clusters for the two lowest redshifts of  $z = 0$  and  $0.07$ .

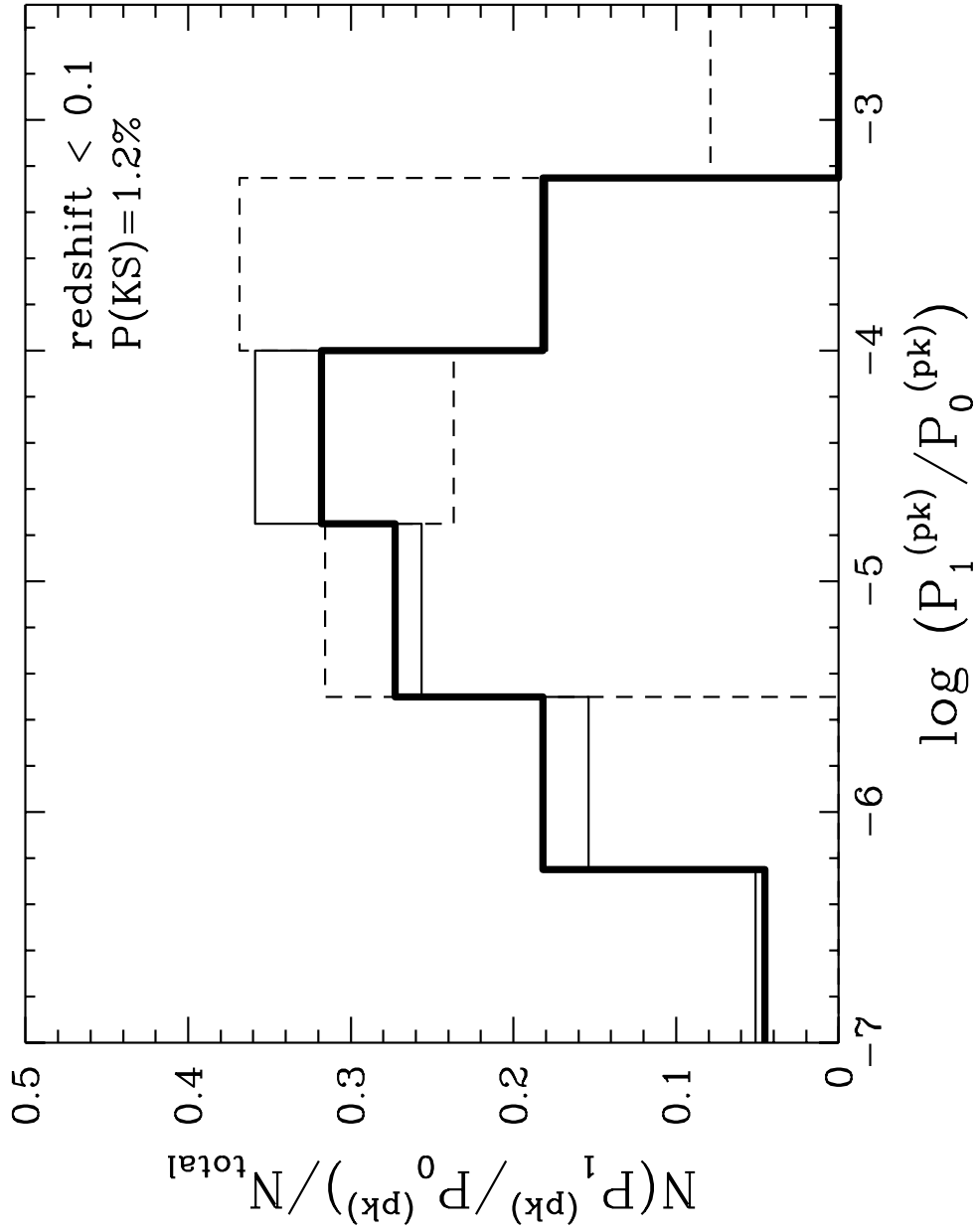


Fig. 8.—



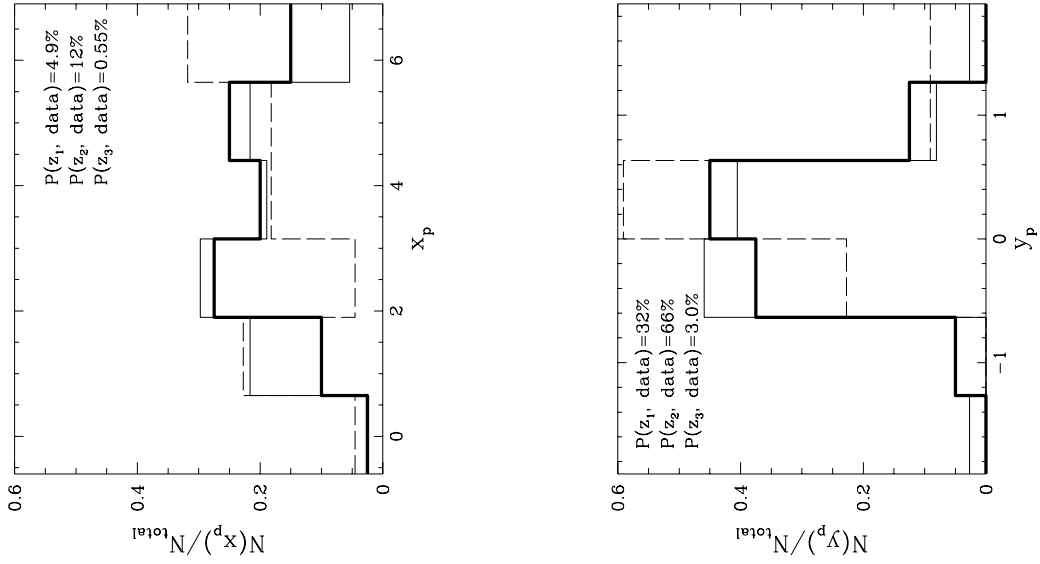
The distribution of clusters in the  $P_3/P_0 - P_2/P_0$  plane are shown. Panel (a) shows the number (normalized to the total number of clusters in the given sample) of clusters with given  $x_p$ . Panel (b) shows the number (normalized to the total) with given values of  $y_p$ . The histograms are plotted as in Figure 7

Fig. 9.—



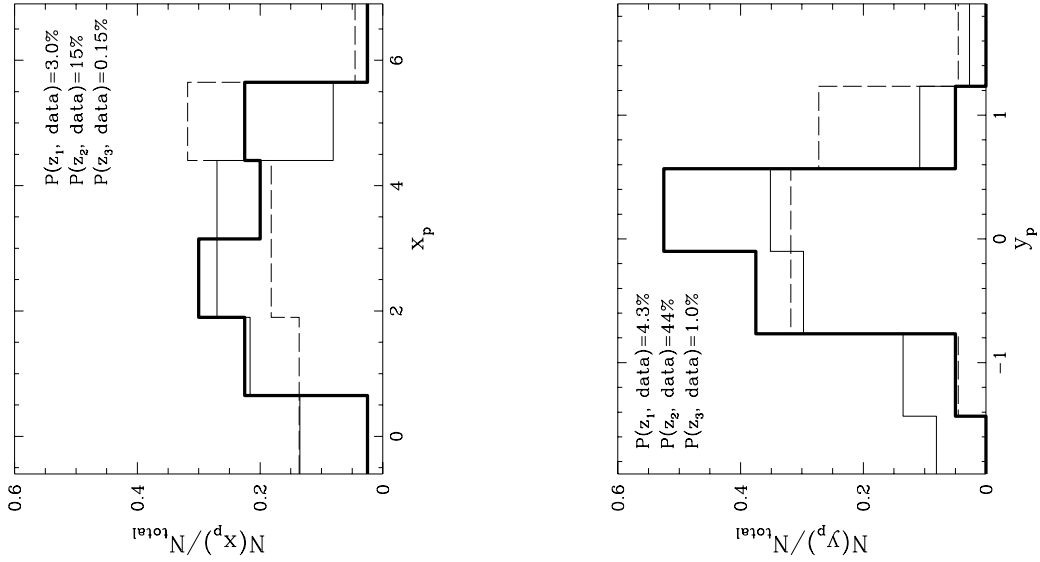
The number of clusters (normalized to the total number in the sample) with  $P_1/P_0$  in the given range is plotted versus  $P_1/P_0$ . The histograms are plotted as in Figure 7.

Fig. 10.—



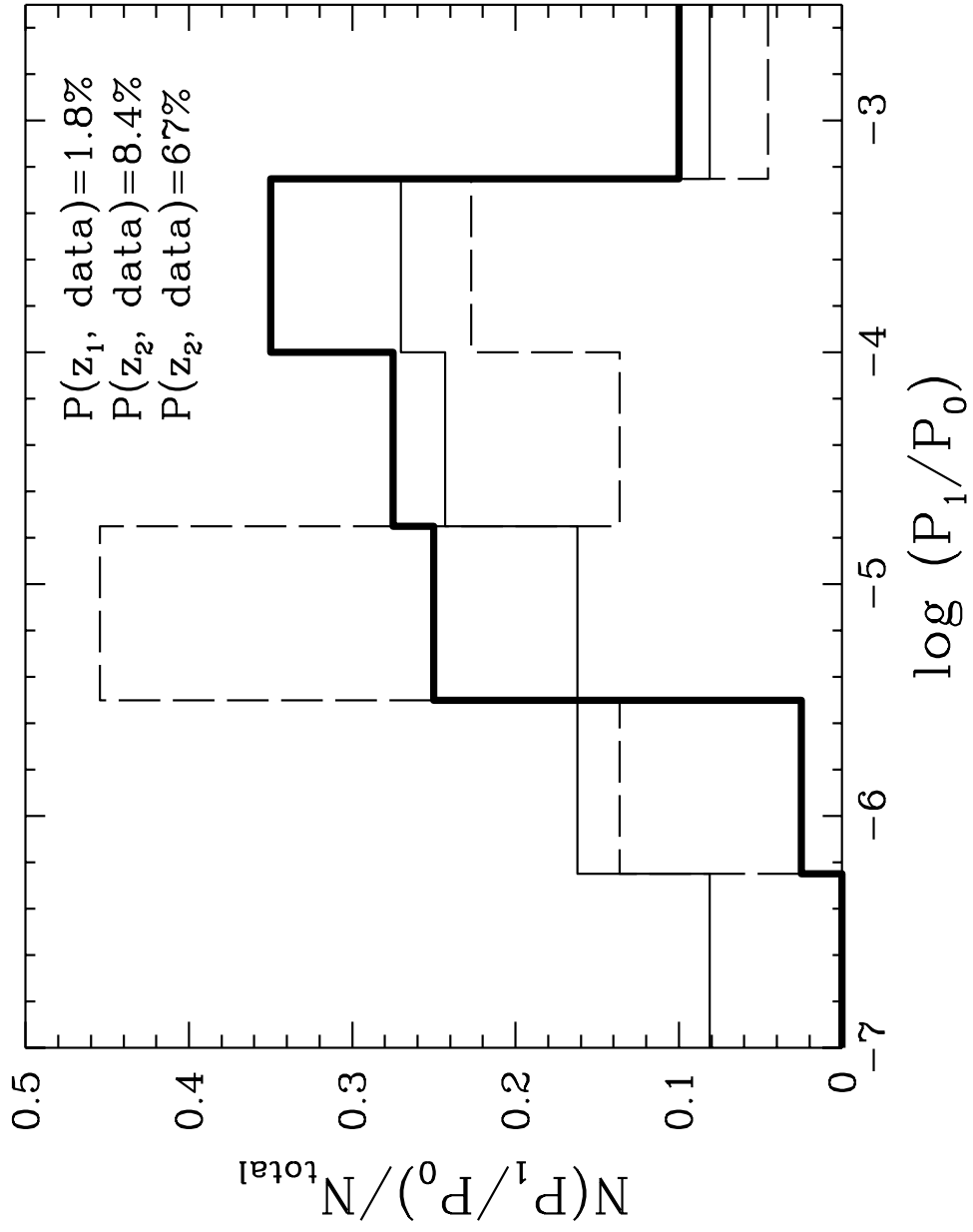
The distribution of clusters in the  $P_4/P_0 - P_2/P_0$  plane are shown in the  $x_p$  (panel [a]) and  $y_p$  directions (panel [b]). The heavy solid histogram gives the distribution for the redshift  $z_1$  ( $z = 0.14$  and  $0.23$ ) clusters, the light solid histogram corresponds to the  $z_2$  clusters ( $z = 0.35$  and  $0.49$ ), and the dashed histogram corresponds to the  $z_3$  clusters ( $z = 0.68$ ).

Fig. 11.—



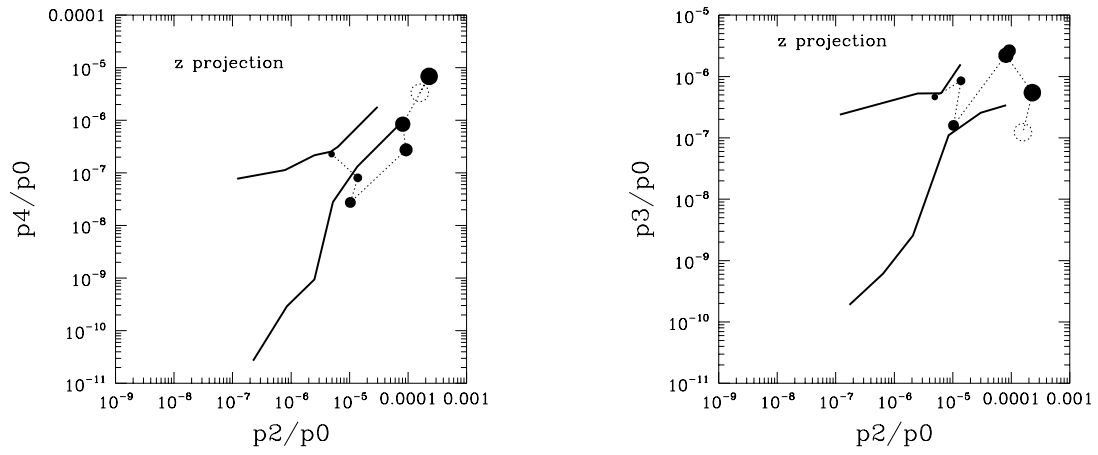
The distribution of clusters in the  $P_3/P_0 - P_2/P_0$  plane are shown in the  $x_p$  (panel [a]) and  $y_p$  directions (panel [b]). Histograms are plotted as in Figure 10.

Fig. 12.—



The number of clusters (normalized to the total number in the sample) with  $P_1/P_0$  in the given range is plotted versus  $P_1/P_0$ . Histograms are plotted as in Figure 10.

Fig. 13.—



Power ratios computed for the projected dark matter distribution along the  $z$  axis for the largest clusters CL1. The ratios are plotted as in Figure 4, where (a) shows  $P_4/P_0$  versus  $P_2/P_0$  and (b) shows  $P_3/P_0$  versus  $P_2/P_0$ . An aperture of 1 Mpc is assumed.